UNIVERSITY OF CALIFORNIA
RIVERSIDE

Nanofabrication and Testing of 1T-TaS_2 Charge-Density-Wave Quantum Devices

A Thesis submitted in partial satisfaction
of the requirements for the degree of

Master of Science

in

Electrical Engineering

by

Jonas Olivier Brown

June 2023

Thesis Committee:

Professor Alexander Balandin, Chairperson
Dr. Fariborz Kargar
Dr. Mahesh Neupane

The Thesis of Jonas Olivier Brown is approved:

Committee Chairperson

University of California, Riverside

Acknowledgments

The text and figures of this thesis, in part, are a reprint of the material as it appears in the following conference proceeding:

Jonas O Brown et al., Charge-density-wave phase transitions in quasi-2D 1T-TaS_2/h-BN heterostructure devices. In Low-Dimensional Materials and Devices 2022, volume 12200, pages 16–23. SPIE, 2022. [1]

ABSTRACT OF THE THESIS

Nanofabrication and Testing of 1T-TaS_2 Charge-Density-Wave Quantum Devices

by

Jonas Olivier Brown

Master of Science, Graduate Program in Electrical Engineering
University of California, Riverside, June 2023
Professor Alexander Balandin, Chairperson

The charge density wave (CDW) phase is a macroscopic quantum phenomenon where the periodic motion of atoms results in a new periodicity of the electron density. Here I present an investigation into the phase transitions and depinning of CDWs in single-crystal 1T-TaS_2 / hBN heterostructure devices. It is known that 1T-TaS_2 reveals multiple CDW phases below and above room temperature. In the nearly commensurate phase domain depinning occurs before the phase transition to the incommensurate phase. This study explores the differences in the depinning process of CDWs between quasi-2D materials and conventional bulk CDW materials with quasi-1D motifs in their crystal structure. Domain depinning in quasi-2D 1T-TaS_2 differs from that of conventional charge-density-wave materials, as it does not exhibit a noticeable abrupt increase in electric current. Rather, domain depinning occurs as current instabilities, revealed by the differential resistance before joule heating. The findings of this study contribute to the understanding of the behavior of CDWs in quasi-2D materials and aid in the optimization of device design.

Contents

List of Figures **viii**

1 Introduction to Charge-Density-Waves **1**
1.1 Instability in the Idealized 1D Atomic Chain 1
1.2 Fermi Surface Nesting 2
1.3 Electron Phonon Coupling 4
1.4 Transitional Metal Dichalcogenides 7

2 Motivating Research **11**
2.1 Early Developments in the Depinning of Quasi One Dimensional Charge Density Wave Materials 11
2.2 Domain Depinning in Quasi Two Dimensional Materials 12
2.3 Thickness Dependent Resistance Studies of Tantalum Disulfide 13

3 Nano Device Fabrication **16**
3.1 Introduction 16
3.2 Cleaning the Silicon Dioxide / Silicon Substrate 17
3.3 Mechanical Exfoliation of Transitional Metal Dichalcogenides 18
3.4 Hexagonal Boron Nitride and Tantalum Disulfide Heterostructures 19
3.4.1 Motivation for Fabricating with Hexagonal Boron Nitride Capping . 19
3.4.2 Viscoelastic Transfer Process 20
3.5 Device Fabrication Steps 22
3.5.1 Designing Alignment Grid 22
3.5.2 Spin Coating Resist Layer 23
3.5.3 Electron Beam Lithography 23
3.5.4 Developing Electron Beam Resist 26
3.5.5 Drawing Small Alignment Markers, Electrodes, and Pads 26
3.5.6 Fabricating Electrodes and Pads 28
3.5.7 Etching Hexagonal Boron Nitride 29
3.5.8 Metal Deposition Using Electron Beam Evaporation 30
3.5.9 Lift-Off Process 30

4 Results and Discussion **33**
4.1 Introduction 33
4.2 Electrical Characterizations of the 1T Phase of Tantalum Disulfide 36
4.3 Thickness Dependent Charge Density Wave Phase Transitions 37
4.4 Depinning of Charge Density Waves in Quasi-2D Materials 39
4.5 Temperature Dependent Study 42
4.6 Conclusions 46

Bibliography **47**

List of Figures

1.1 Peierls Transition: Above threshold transition temperature ion cores are in their original lattice spacing a where there is no energy band gap (metallic phase). Below this threshold temperature, the ion cores move closer to one nearest neighbor and further from the other nearest neighbor. This new periodicity in the lattice causes a splitting in the energy band gap as CDWs become present causing a periodic fluctuation in electron density [2]. 3

1.2 The acoustic phonon dispersion of 1D, 2D and 3D metals. Here the reduced phonon frequency seen at $2k_F$ is due to the temperature dependence of $\chi(q, T)$ which is weaker for higher dimensions [2]. 6

1.3 TaS_2 Polymorphs. Blue spheres represent the Tantalum atoms and yellow spheres represent the Sulfur atoms. (a) the 1T phase has 1 trigonal layer in the unit cell. (b) The 2H phase has two hexagonal layers in the unit cell. . 8

1.4 Three dominant CDW phases in 1T-TaS_2. (a) In the commensurate phase, the SD clusters hold perfect translational symmetry with the underlying lattice and are uniformly distributed. This symmetry causes the material to exhibit a Mott insulating state. (b) The NC-CDW phase has some regions where the CDW is commensurate with the underlying lattice and some regions where it is not. This state is interesting because it exhibits domain depinning where the C-CDW domains will change size, position, and shape with respect to one another, which will be discussed in detail later. (c) Finally, in the IC-CDW phase, the CDW holds no symmetry and is incommensurate with the underlying lattice. This state has the highest conductivity of the three listed states. 10

2.1 The resistance vs temperature is shown for 1T-TaS_2 devices of varying thickness. Dotted lines represent the heating cycle and solid lines represent the cooling cycle. Phase transitions are shown by the hysteresis. For thin devices ($\leq$ 10 nm) there is no transition to the C-CDW state. However, for thick devices ($\geq$ 10 nm) there is a noticeable transition to the C-CDW state. Thinner devices have higher resistance. 14

3.1 The transfer system (a) consists of two stages: the sample holder at the bottom and the hBN on the PDMS stamping layer at the top stage. The movement of both stages is precisely controlled using micromanipulators, which enables successful transfer. (b) Top view showing the clear PDMS on a glass slide and the SiO_2/Si substrate with 1T-TaS_2 below. 20
3.2 (a) A thin flake of hBN exfoliated on PDMS (b) A thin flake of 1T-Ta_2 exfoliated onto SiO_2/Si (c) The thin flake of 1T-Ta_2 capped with hBN after the transfer process. 21
3.3 Design CAD is used to create the alignment grid, the small alignment marks, the electrodes, and the pads (a) Small alignment marks (teal) and center "01". The dark blue ticks show the alignment grid and the teal rectangles show the area that will be scanned to assign the alignment marks. (b) An optical image of the device (after alignment marks have been made with EBL and revealed after development) is used to assign the center and create the alignment marks, electrodes, and pads. Here the electrodes are placed on the 1T-TaS_2 flake capped with hBN and connected to the larger square pads using the alignment grid as a reference. (c) Zooming in gives a closer look at the electrodes (yellow dashed lines) on the 1T-TaS_2/hBN heterostructure. Dashed lines represent areas that will be exposed to the EBL. 28
3.4 (a) A thin flake of 1T-TaS_2 (thin purple) on SiO_2/Si is capped with hBN (teal). PMMA A4 is spin-coated and baked on the substrate. Alignment marks are written with EBL and developed (b) A pattern for the electrodes and the pads is written using EBL and revealed after development. Pink regions reveal the SiO_2 and teal regions reveal the hBN through the PMMA. (c) After ALE the patterns show a uniform color understanding that the hBN has been etched through properly (d) The final optical image of a 1T-TaS_2 device capped with hBN after electrodes and pads are written with EBL, developed, Ti/Au contacts are deposited with EBE and PMMA is removed with acetone. 32

4.1 Crystal structure of 1T-TaS_2 (left panel) and schematic of the atoms structuring in the nearly-commensurate CDW phase (NC-CDW) (right panel). This figure is reprinted with permission from Jonas O Brown et al., Charge-density-wave phase transitions in quasi-2D 1T-TaS_2/hBN heterostructure devices. In Low-Dimensional Materials and Devices 2022, volume 12200, pages 16–23. SPIE, 2022 [1]. 35

4.2 (inset) Schematic of the device, indicating 1T-TaS_2 layer (green) on a heavily p+ doped Si (grey) with 300 nm thick SiO_2 layer (violet). The layer of 1T-TaS_2 is capped with hBN (blue). The source-drain contacts (gold) are patterned using the EBL followed by the ALE to remove the hBN layer beneath the contacts. The contacts are made using the electron beam evaporation of Ti / Au with 10 nm / 100 nm thickness. I-V characteristics of a 1T-TaS_2/hBN CDW device from 100 K to 350 K. One can see the characteristic hysteresis and resistivity change induced by passing an electrical current via the device channel. This figure is reprinted with permission from Jonas O Brown et al., Charge-density-wave phase transitions in quasi-2D 1T-TaS_2/hBN heterostructure devices. In Low-Dimensional Materials and Devices 2022, volume 12200, pages 16–23. SPIE, 2022 [1]. 37
4.3 (a) I–V characteristics of the same device at room temperature. The arrows show the voltage sweep direction. The hysteresis window is defined as V_H – V_L. The inset shows the current below V_H. (b) Temperature-dependent switching voltage confirms the CDW effect. Note that V_H and V_L are proportional to $(1 - T/T_{NC-IC})^{1/2}$ [3]. This figure is reprinted with permission from Jonas O Brown et al., Charge-density-wave phase transitions in quasi-2D 1T-TaS_2/hBN heterostructure devices. In Low-Dimensional Materials and Devices 2022, volume 12200, pages 16–23. SPIE, 2022 [1]. 38
4.4 Domain depinning of CDWs for different temperatures. Panels (a) and (b) depict differential I-V characteristics as a function of bias voltage for 77 K and 300 K, respectively. The V_{OF} indicates the domain depinning in the forward bias and V_{OR} is the onset in the reverse bias. This figure is reprinted with permission from Jonas O Brown et al., Charge-density-wave phase transitions in quasi-2D 1T-TaS_2/hBN heterostructure devices. In Low-Dimensional Materials and Devices 2022, volume 12200, pages 16–23. SPIE, 2022 [1]. 41
4.5 Domain depinning of CDWs for different temperatures. Panel (a) and (b) compare the domain depinning voltage shifts at a temperature near C-CDW – NC-CDW transition of bulk 1T-TaS_2 in the heating cycle. As the temperature switches from 210 K to 220 K, V_{OF} shifts about $\sim$ 40 mV and V_{OR} decreases for almost $\sim$ 270 mV. This figure is reprinted with permission from Jonas O Brown et al., Charge-density-wave phase transitions in quasi-2D 1T-TaS_2/hBN heterostructure devices. In Low-Dimensional Materials and Devices 2022, volume 12200, pages 16–23. SPIE, 2022 [1]. 41
4.6 Contour plot showing the temperature dependence of the phase transition during the heating cycle for a thin device $\leq 10nm$. The NC - IC-CDW phase transition is shown as the boundary between the green and the red region. . 43
4.7 Threshold of domain depinning as a function of temperature for both thick [$\sim$ 30 nm] (green) and thin [$\sim$ 15 nm] (brown) devices. Error is understood by the uncertainty in determining the onset of the domain depinning. . . . 45

Chapter 1

Introduction to Charge-Density-Waves

1.1 Instability in the Idealized 1D Atomic Chain

The original theory of charge density waves (CDWs) came from Peierls' understanding of instability in an ideal 1D periodic chain of equally spaced atoms. In many materials with quasi-1D crystal structures, typically metals where we have strong bonds in one dimension, it becomes energetically favorable to undergo lattice deformation below a critical temperature. This transition is the Peierls transition. Here the periodic motion of atoms results in a new periodicity of the electron wave function and correspondingly the electron density. As a result of this new periodicity, we have a band gap opening. This is the fundamental concept of a CDW and is shown in Figure 1.1 where a represents the lattice spacing. When there is a lattice distortion, where every other ion moves closer to one

neighbor and further than the other, (in the 1D case provided in Figure 1.1) the period of the ion cores will eventually double transitioning from a to $2a$ opening the energy bandgap (the required energy for an electron to break free from its bound state). This opening causes a phase transition in the material transitioning it from a conducting to an insulating state. It should be noted that the electron wavefunction is present in these materials over a significant distance meaning that a CDW is a macroscopic quantum phenomenon with a large coherence length [4]. The field of Charge Density Waves which was first popularized in the 1970s and 1980s is experiencing a rebirth driven by the emergence of new material systems and the realization that these materials transition through a CDW phase above room temperature [5–7].

1.2 Fermi Surface Nesting

In the 1930s Peierls prophesied that CDWs would form due to the instability of an ideal 1D chain of atoms causing a reconstruction of the lattice. Later in 1959, Dr. Walter Kohn coined the term Fermi Surface Nesting (FSN) for a simultaneous softening of coherent lattice vibrations otherwise known as phonon softening. Simply put, FSN occurs when there are many filled and unfilled states on the Fermi surface that are separated in k-space equally by vector q_{CDW} (the CDW wavevector). A phonon of the same magnitude will then scatter the electrons from the filled to the unfilled states elastically since all the points on the Fermi surface have the same energy ϵ_F.

However, in quasi-2D TMDs, it has been argued that only a small fraction, if any, of the observed charge ordering phase transitions are truly from Peierls instability

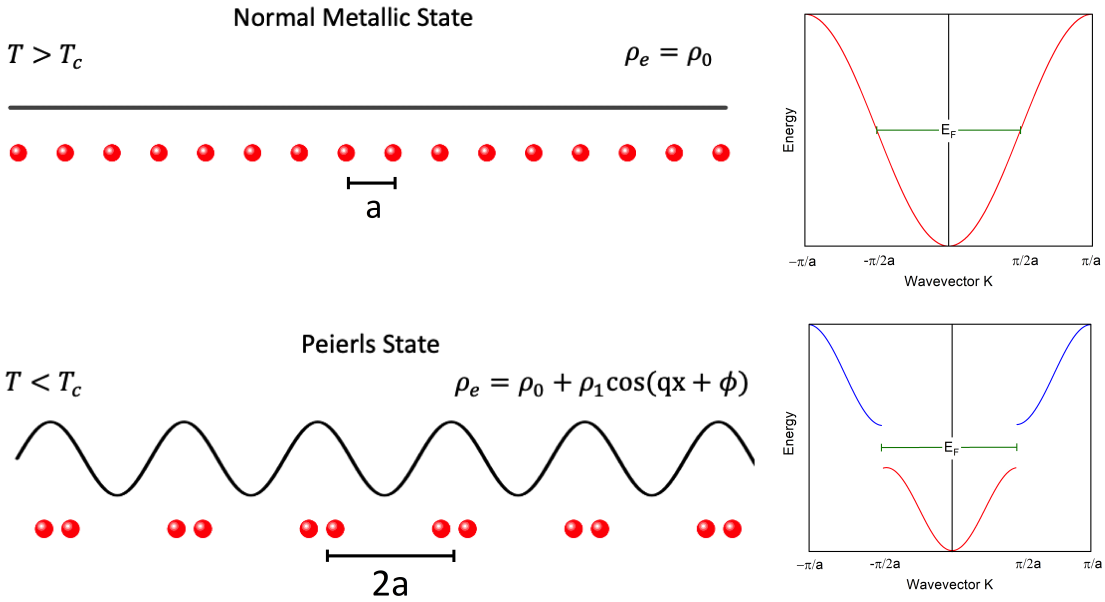

Figure 1.1: Peierls Transition: Above threshold transition temperature ion cores are in their original lattice spacing a where there is no energy band gap (metallic phase). Below this threshold temperature, the ion cores move closer to one nearest neighbor and further from the other nearest neighbor. This new periodicity in the lattice causes a splitting in the energy band gap as CDWs become present causing a periodic fluctuation in electron density [2].

because these instabilities are easily destroyed by small deviations from perfect nesting conditions. There is growing evidence to support the momentum dependence of electron-phonon coupling (EPC) to determine the characteristic CDW phase. In 2D TMDs such as $NbSe_2$ and $TaSe_2$ it has been shown that the CDW phase transitions are actually structural phase transitions from the commensurate and incommensurate lattice transitions. Here it is reported the energy gain comes from the lowering of already filled states away from the Fermi energy and not from removing states from the Fermi energy as proposed in the FSN scenario [2]. Although it is possible for the CDW state to be tied to FSN if the dimensionality is truly reduced there are no true 1D systems in nature. If ions can move in 2D the lowest energy state is a zigzag chain where the electronic gap anticipated by Peierls is missing [8].

1.3 Electron Phonon Coupling

One of the key factors that govern the behavior of CDW materials is the interaction between the electrons and the lattice vibrations, which is described by the electron-phonon coupling equation. This equation provides a quantitative description of the interaction between the electrons and the lattice vibrations, which is mediated by the exchange of phonons. The interaction can lead to the formation of CDWs, as well as other phenomena such as superconductivity and metal-insulator transitions. Understanding the electron-phonon coupling in CDW materials is therefore crucial for developing a comprehensive understanding of their properties and behavior.

The Hamiltonian describing electron and phonon states in a system can be written

in second quantization form as

$$H = H_{el} + H_{ph} = \sum_k \epsilon_k a_k^\dagger a_k + \sum_k \hbar\omega_q b_q^\dagger b_q$$

where $a, a^\dagger, b, b^\dagger$ are the creation and annihilation operators for respective phonon and electron states represented by indices k and q. If we consider the electron-phonon interactions we have the Frohlich Hamiltonian:

$$H = H_{el} + H_{ph} + H_{el-ph}$$

$$H = \sum_k \epsilon_k a_k^\dagger a_k + \sum_k \hbar\omega_q b_q^\dagger b_q + \sum_{k,q} g_{k,k+q} a_{k+q}^\dagger a_k (b_{-q}^\dagger + b_q)$$

where $g_{k,k+q}$ represents the electron-phonon coupling coefficient. The equation of motion then becomes

$$\ddot{Q}_q = -\omega_q^2 Q_q - g(\tfrac{2\omega_q}{M\hbar})^{1/2}\rho_q$$

where $\ddot{Q}_q$ represents the acceleration of the phonon wavevector, $\rho_q = \sum_k a_{k+q}^\dagger a_k$ is the Fourier component of electron density and g is the electron-phonon coupling coefficient that is independent of q. From this, we can find the phonon frequency

$$\Omega_q^2 = \omega_q^2 + \tfrac{2\omega_q g^2}{\hbar}\chi_q$$

Here $\Omega(k)$ is the re-normalized phonon frequency after the perturbation and $\chi(q)$ is the Lindhard response function:

$$\chi_q = \int \frac{f_k - f_{k+q}}{\epsilon_k - \epsilon_{k+q}} dk$$

where f_k is the Fermi distribution function and ϵ_k and $\epsilon_{k,q}$ are the electronic energy states. The phase transition is defined by the temperature where $\Omega_q \to 0$. This is shown in Figure

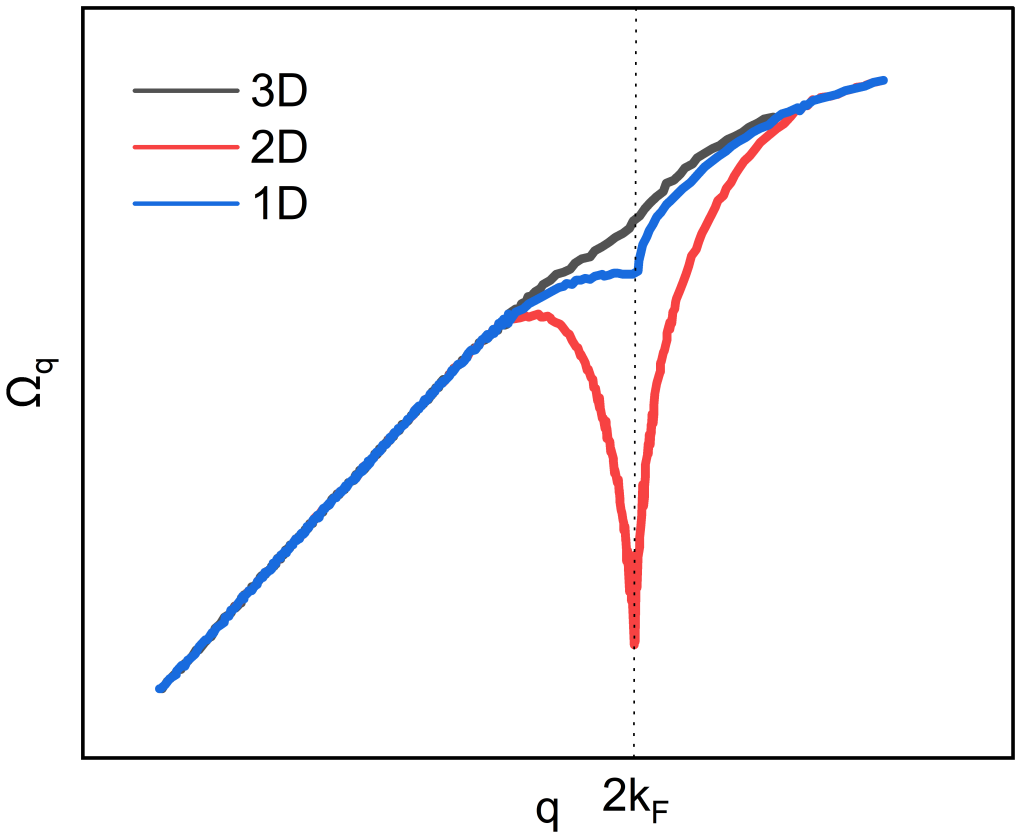

Figure 1.2: The acoustic phonon dispersion of 1D, 2D and 3D metals. Here the reduced phonon frequency seen at $2k_F$ is due to the temperature dependence of $\chi(q,T)$ which is weaker for higher dimensions [2].

1.2 where the temperature dependence of $\chi(q,T)$ is weaker for higher dimensions and the reduction of phonon frequencies is less significant. Here we understand that even in 3D metals there is a reduction in the phonon frequency due to the presence of CDWs.

Phonon softening occurs when the re-normalized phonon frequency dips sharply at certain values of q. If the frequency drops to zero the result is a static phonon with finite wave-vector q_{CWD}. Here the displacement of the ions due to this phonon is fixed in time

resulting in a periodic distortion of ions and charge density with wave-vector q_{CWD}. This understanding clarifies why CDW transitions are noticed in quasi-1D and 2D materials [2].

1.4 Transitional Metal Dichalcogenides

Transitional Metal Dichalcogenides (TMDs) have attracted great interest as functional materials for a variety of uses in the field of superconductivity, solar cells, oscillator circuits, neural networks, and transistors [9–12]. TMDs (MX_2, where M refers to the transitional metal and X_2 refers to the two chalcogen atoms) come in a variety of different structural polytypes. Often the ground state polytype depends on the transitional metal. For example, TMDs with a transitional metal in group 4 of the periodic table exist naturally in the 1-T polytype. TMDs with a transitional metal in group 6 exist naturally in the 2H polytype. Groups 4-7 exist in layered quasi-1D and 2D structures in which the layers are separated by Van der Waals bonds. These layered structures make it easy to mechanically cleave thin layers down to the atomic limit. Later there will be a discussion about the interesting physics understood from these atomically thin structures. Groups 8-10 exist in nonlayered 3D structures and will not be discussed any further. When referring to the polytype of a TMD the number represents the number of layers in the unit cell and the letter represents the structure. For example, 1T has one trigonal layer in the unit cell, 2H has two hexagonal layers in the unit cell, and 3R has three rhombohedral layers in the unit cell. The 1T and 2H polymorphs of Tantalum Disulfide are shown in Figure 1.3.

Transitional Metal Dichalcogenides (TMDs) have gained interest due to their ability to transform from metallic to insulating. 1T-TaS_2 is unique in that it is understood to

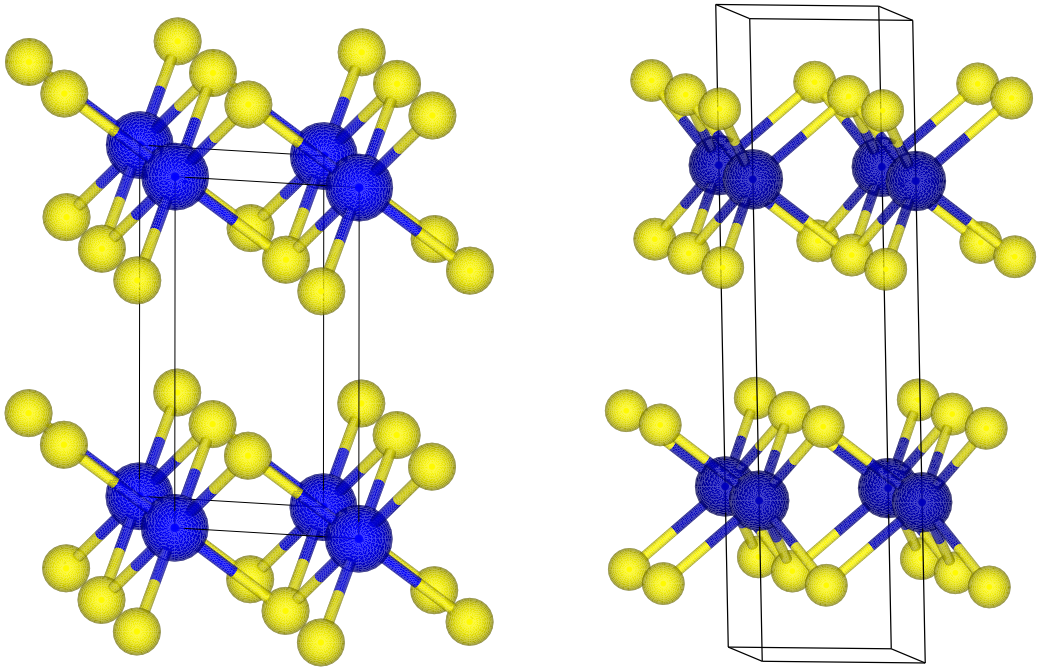

(a) (b)

Figure 1.3: TaS_2 Polymorphs. Blue spheres represent the Tantalum atoms and yellow spheres represent the Sulfur atoms. (a) the 1T phase has 1 trigonal layer in the unit cell. (b) The 2H phase has two hexagonal layers in the unit cell.

be a correlation-driven insulator with a dependency on the ordering of the individual layers as well as the symmetry contained in an individual layer. This material undergoes three structural transitions associated with CDWs. The Incommensurate-CDW (IC-CDW) is a metallic charge density wave state and does not contain coherent structural symmetry with the charge density wave. A semi-metallic state is realized upon the ordering of the "Star of David" (SD) domains and is called the Nearly Commensurate-CDW state (NC-CDW). The third state is a Commensurate-CDW (C-CDW) phase 1T-TaS_2 with perfect translational symmetry transitioning the material to an insulating state. Figure 1.4 depicts these three states from a top view of the lattice formation.

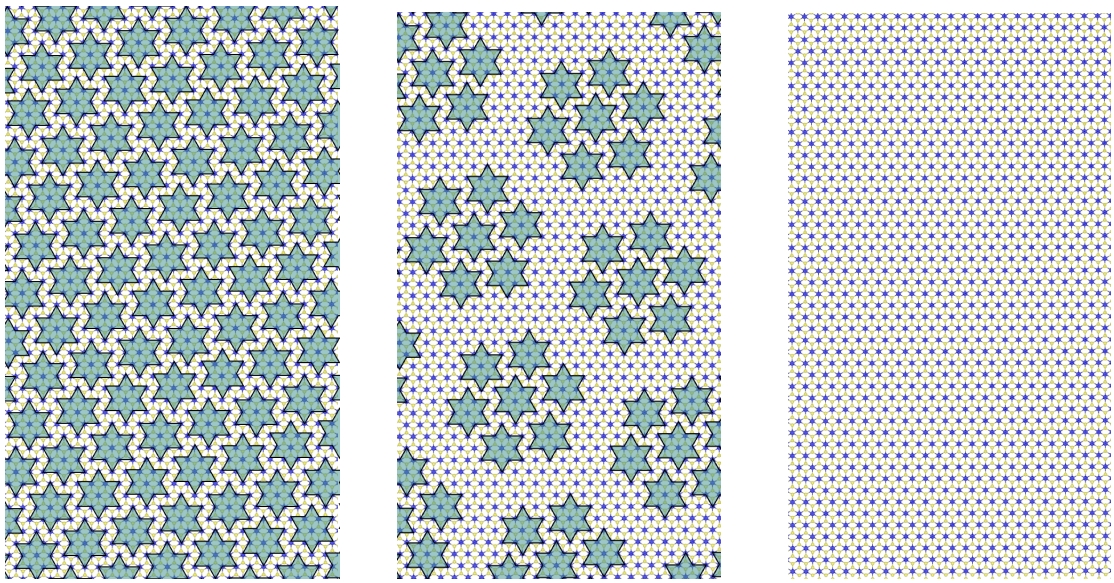

(a) (b) (c)

Figure 1.4: Three dominant CDW phases in 1T-TaS_2. (a) In the commensurate phase, the SD clusters hold perfect translational symmetry with the underlying lattice and are uniformly distributed. This symmetry causes the material to exhibit a Mott insulating state. (b) The NC-CDW phase has some regions where the CDW is commensurate with the underlying lattice and some regions where it is not. This state is interesting because it exhibits domain depinning where the C-CDW domains will change size, position, and shape with respect to one another, which will be discussed in detail later. (c) Finally, in the IC-CDW phase, the CDW holds no symmetry and is incommensurate with the underlying lattice. This state has the highest conductivity of the three listed states.

Chapter 2

Motivating Research

2.1 Early Developments in the Depinning of Quasi One Dimensional Charge Density Wave Materials

In one of the first manifestations of CDWs it was shown that below a certain threshold field, the current is weak and governed by single-particle electron conduction. Above a certain threshold the CDW starts to slide, the current increases dramatically and there is an emergence of an AC component which is characteristic of the periodicity of CDW. One can apply a DC bias leading to an AC response which was originally understood as Narrow Band Noise but is just the AC response of the material. It should be noted the CDW does not slide immediately because it is pinned by defects and impurities in the crystal lattice [5].

The question of the temperature dependence of this pinning threshold is important because, in the conventional theory, one understands the wave can only propagate when it

is incommensurate with the underlying crystal lattice. Typically, at low temperatures, the wave is Commensurate with the underlying structure, and it becomes prohibitively energetically expensive to move it. In many cases, as the temperature is lowered the threshold field required to depin the CDW from the underlying lattice increases [7]. In Tetrathiafulvalene-tetracyanoqinodimethane (TTF-TCNQ) the phase transition to the C-CDW phase is around 50 K. At lower temperatures in the C-CDW phase, a larger electric field is required to depin the charge density wave. However, there are some acceptations to this. For example, In blue bronze, the threshold field decreases with the decrease in temperature even in the commensurate phase below 100 K [6].

2.2 Domain Depinning in Quasi Two Dimensional Materials

It is also important to understand the depinning of CDWs in quasi-2D crystals. This phenomenon of domain depinning shows a loss of the one-to-one relationship between the C-CDW domains in the NC-CDW phase as they move relative to one another, and change shape and size. In a recent discovery by Mohammadzadeh et al. 1/f noise was used to understand the onset of domain depinning in 1T-Ta_2 [13]. One can adapt the model of a sliding CDW in the quasi-1D scenario to the quasi-2D case. Here the velocity is $v = f\lambda$ where f is the average frequency of wave propagation and λ is the CDW wavelength equal to one edge of the C-CDW super-cell $\lambda = \sqrt{13}a_0$. Here $a_0 = 3.365A$ is the in-plane lattice constant in the normal phase. Thus we can find the area of the super-cell as $A = \lambda^2\frac{\sqrt{3}}{2} = 1.32nm^2$. From this, we can understand the current density as $J_{CDW} = env$ where e is the charge of an electron, and n is the number of electrons per unit cell of

the C-CDW 2D super-cell. In this case, there is one electron per unit cell so we can take $n_{2D} = \frac{1}{\lambda^2}\frac{2}{\sqrt{3}} = 7.8 \times 10^{13} cm^{-2}$ and $n_{3D} = \frac{n_{2D}}{c_0} = 1.3 \times 10^{21} cm^{-3}$ where c_0 is the out of plane lattice constant. This gives the current density associated with the commensurate islands as

$$J_{CDW} = \frac{ef}{c_0 \lambda} = 1.5 A/cm^2$$

assuming the frequency $f = 60kHz$ corresponds to a voltage of $V = 0.45V$. This shows the calculated current density associated with the commensurate islands is a good estimate assuming the bulge in the noise spectrum results from the movement of the C-CDW islands or the discommensurations (domain walls) separating the islands. We can use this current density to understand the magnitude of current associated with the onset depinning of CDWs [13].

2.3 Thickness Dependent Resistance Studies of Tantalum Disulfide

Other studies have shown that below temperatures of 183 K, there is a noticeable transition in the resistance versus temperature of 1T-TaS_2 showing the transition from NC-CDW to C-CDW. This transition is understood to be dependent on the thickness of the material used. Figure 2.1 shows the dependence on thickness with the transition to the C-CDW state. The NC-CDW to C-CDW transition is suppressed for devices with thicknesses less than 10 nm. Dotted lines are used to show the heating cycle whereas solid lines are used to show the cooling cycle. Hysteresis is formed from the difference in phase transition

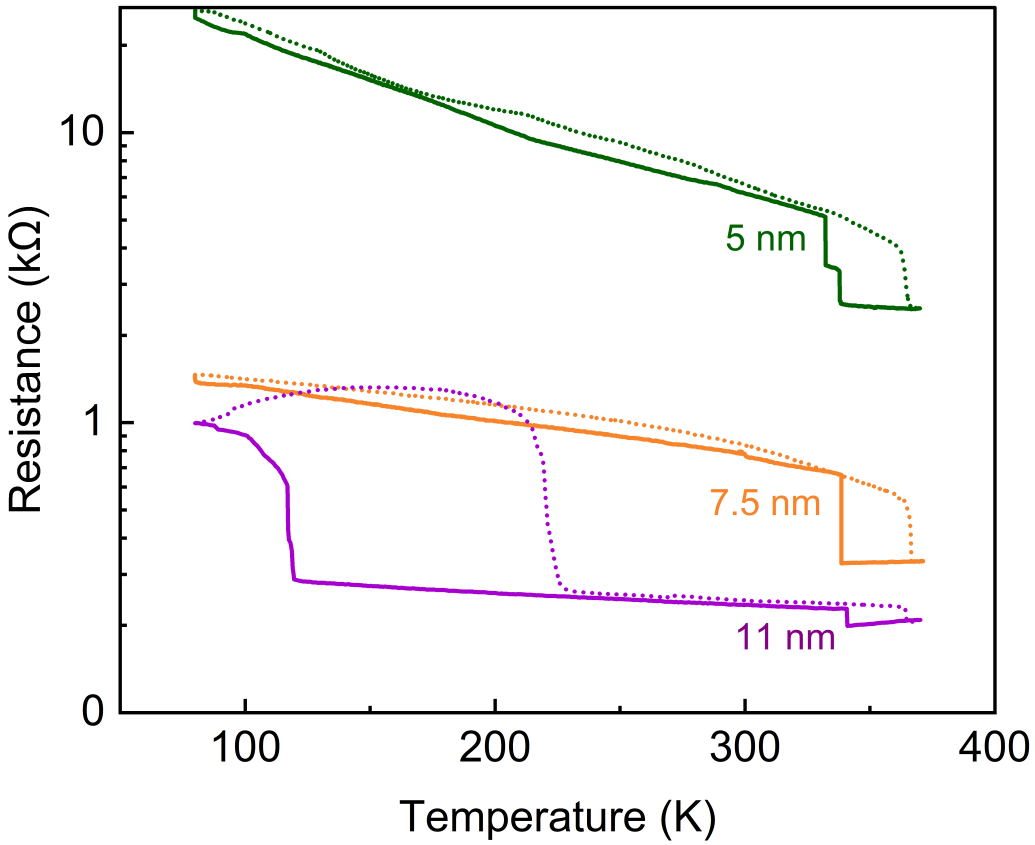

Figure 2.1: The resistance vs temperature is shown for 1T-TaS_2 devices of varying thickness. Dotted lines represent the heating cycle and solid lines represent the cooling cycle. Phase transitions are shown by the hysteresis. For thin devices ($\leq$ 10 nm) there is no transition to the C-CDW state. However, for thick devices ($\geq$ 10 nm) there is a noticeable transition to the C-CDW state. Thinner devices have higher resistance.

temperatures for the heating and cooling cycles.

This result is consistent with the resistance versus temperature analysis for 1T-TaS_2 with varying thicknesses [14–16]. In bulk single crystals, there is a suppression of the resistance versus temperature hysteresis window in the NC-CDW to IC-CDW transition but an increase in the hysteresis window in the C-CDW to NC-CDW transition and visa-versa for thinner flake materials. It is important to note here the influence of Joule Heating as we decrease the thickness of the 1T-TaS_2. As the thickness of the 1T-TaS_2 decreases the window opens and the change in resistance suppresses. In other words, the onset temperature for the C-CDW to NC-CDW transition in the heating cycle begins earlier. In the cooling cycle, the sample moves from a higher temperature where Joule heating is enhanced. The transition in resistance occurs at a higher temperature for this reason. This demonstrates that 1T-TaS_2 must be thicker than 10 nm to realize all transitions from the C-CDW to the NC-CDW to the IC-CDW. 1T-TaS_2 with thickness less than 10 nm will be able to show the NC-CDW to the IC-CDW transition until about 2.5 nm in which there is no noticeable transition and the flake resides in an insulating phase independent of temperature [14–16].

Chapter 3

Nano Device Fabrication

3.1 Introduction

Here, I briefly outline CDW device fabrication procedures. First bulk 1T-TaS_2 crystals are grown by the chemical vapor transport (CVT) method [17–22]. The composition and structure are confirmed by X-Ray Diffraction (XRD), Energy Dispersive Spectroscopy (EDS), and Raman Spectroscopy. Thin films of the material are then mechanically exfoliated from the 1T-TaS_2 crystals onto Si/SiO_2 substrates. Then layers of 1T-TaS_2 are capped with electrically insulating thin films of hBN with a few nm thicknesses to protect from degradation. The source-drain contacts are patterned with the Electron Beam Lithography (EBL) followed by an Atomic Layer Etching (ALE) step to remove the hBN layer underneath the contacts. Finally, the evaporation of Ti/Au is used to fabricate device structures. The fabricated devices consist of 1T-TaS_2 channels with thicknesses in the range of 6 nm – 40 nm.

3.2 Cleaning the Silicon Dioxide / Silicon Substrate

To prevent crystal detachment during subsequent fabrication steps, a cleaning procedure is introduced for the SiO_2/Si substrate with a 300 nm oxide layer. The first step involves cutting the silicon wafers into small pieces. This is done with a diamond scribe pen because although SiO_2 is a relatively hard material diamond has a higher hardness and is able to score the SiO_2 cleanly. The scored regions break easily with applied pressure. These $1cm \times 1cm$ squares are then subjected to a sequence of treatments where they are first sprayed with acetone (to remove the debris from scoring), then they are placed in a bath of acetone and sonicated for 10 minutes. Sonication helps remove the debris from the scoring that still remains even after rinsing with acetone. The sonicator uses high-frequency sound waves to dislodge small particles on the surface (the frequency used is 40 kHZ). After the substrate is rinsed with isopropyl alcohol (IPA), and dried with nitrogen gas. After drying, the SiO_2/Si pieces undergo oxygen plasma treatment for 10s at a power of 50 W using an Atomic Layer Etcher (ALE). Inductively Coupled Plasma (ICP) with forward power of 2000 W is used to generate a high-density plasma. The plasma is created by applying a high-frequency electromagnetic field to a gas, typically a mixture of a reactive gas (O_2 50 sccm) and an inert gas (N_2), inside a vacuum chamber. The reactive gas reacts with the material to be etched, while the inert gas is used to control the ion energy and prevent sputtering. The ions in the plasma are accelerated by the electric field and collide with the material surface, removing atoms or molecules and allowing for precise atomic layer removal. The ALE employs a strong radio frequency (RF) electromagnetic field to the wafer platter producing a plasma. As a result, the positive ions migrate towards the wafer platter and

interact with the samples, facilitating substrate cleaning and enhancing the probability of successful crystal attachment to the surface in subsequent steps.

3.3 Mechanical Exfoliation of Transitional Metal Dichalcogenides

1T-TaS_2 belongs to the Transition Metal Dichalcogenides (TMDs) family, which are characterized by their layered structures where layers are held together by weak van der Waals forces. As a result, mechanical exfoliation is a suitable method to obtain thin layers of 1T-TaS_2 from bulk to nanometer scales. In this study, the bulk 1T-TaS_2 flakes were purchased from HQ Graphene and were made thin using a mechanical exfoliation technique [23]. To exfoliate the bulk material, it is first placed on Nitto tape. The tape is then folded back onto itself to increase the coverage of the exfoliated material on the tape. Subsequently, another strip of tape is placed on top of the first strip, and the new strip is slowly removed at a large angle to promote the exfoliation of thin flakes. This sequence of steps is repeated until the desired flake thickness and coverage are achieved. When finished the Nitto tape is placed on the Si / SiO_2 substrate and slowly removed, again at a large angle from the surface. In particular, for 1T-TaS_2 it can be useful to exfoliate onto Si / SiO_2 at 60 C (333 K) because this is slightly below the phase transition of the material to the IC-CDW phase (a more metallic phase with more charge carriers) requiring less activation energy to separate individual layers. The purple-colored flakes were found to be much thinner compared to the brighter and gold-colored ones, with thicknesses ranging under 12 nm [24]. Optically the difference can be seen in Figure 3.2 (b). These thin purple flakes

are particularly desirable in this study as they offer better control and manipulation over the nearly commensurate to incommensurate charge density wave phase (NC - CDW) [25]. The thickness of the purple 1T-TaS_2 crystals can be estimated to be under 12 nm based on the color contrast of the optical microscopy images which has roughly been confirmed with Atomic Force Microscopy AFM [24].

3.4 Hexagonal Boron Nitride and Tantalum Disulfide Heterostructures

3.4.1 Motivation for Fabricating with Hexagonal Boron Nitride Capping

Hexagonal boron nitride (hBN) is a 2D material composed of boron and nitrogen atoms arranged in a hexagonal honeycomb structure, with a wide band gap. The layers of hBN are stacked on top of each other through van der Waals forces making it easy to mechanically cleave into thin layers. Since hBN is an insulator, with a relatively high thermal conductivity compared to other insulating materials and a similar lattice geometry to many low-dimensional metals it is a great candidate for capping [26, 27]. The similar geometry allows there to be reduced strain and defects on the interface of the two materials. Therefore, in this work, hBN has been employed as a protective layer for 1T-TaS_2. In particular, 1T-TaS_2 has been shown to oxidize when left in ambient conditions for an extended period of time. DFT calculations show that the edges of 1T-TaS_2 are susceptible to oxidation in air, which could result in the loss of CDW superlattice phonons [28]. Thus hBN is also used to help to protect devices from oxidation as well as other contaminants that may be present before and after the fabrication process.

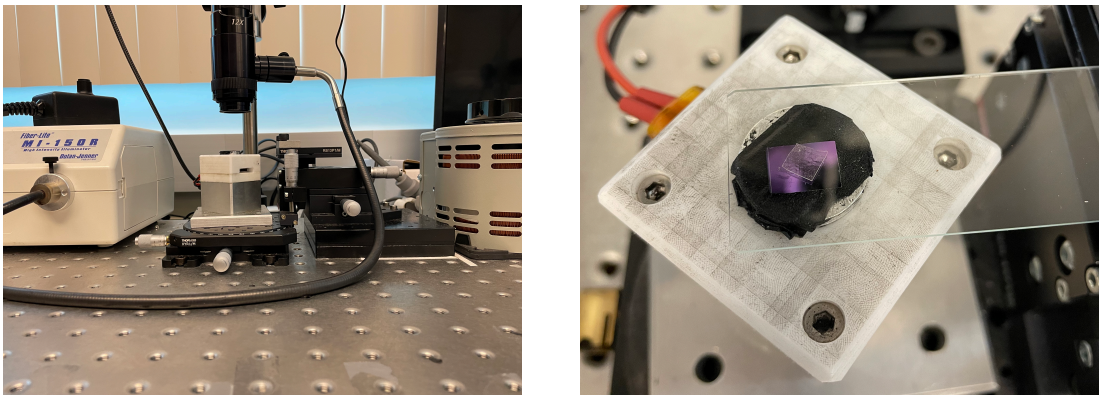

(a) (b)

Figure 3.1: The transfer system (a) consists of two stages: the sample holder at the bottom and the hBN on the PDMS stamping layer at the top stage. The movement of both stages is precisely controlled using micromanipulators, which enables successful transfer. (b) Top view showing the clear PDMS on a glass slide and the SiO_2/Si substrate with 1T-TaS_2 below.

3.4.2 Viscoelastic Transfer Process

Thin flakes (a few nanometers) of hBN are obtained through mechanical exfoliation, resulting in a blue or greenish-colored material which is then transferred onto the 1T-TaS_2 crystal. The transfer is accomplished through a dry viscoelastic stamping method, where a polymer: polydimethylsiloxane (PDMS) is used as the stamp. The two-stage dry transfer system contains a top stage holding the PDMS layer controlled by a micromanipulator, and the sample located on the bottom stage. The capping step should be carried out immediately after exfoliation to prevent oxidation of the 1T-TaS_2. Figure 3.1 illustrates the setup of the all-dry transfer system used in this thesis.

First, a small square of PDMS is cut and placed onto a glass slide [25]. The hBN is then mechanically exfoliated and deposited onto a transparent PDMS layer. The substrate with the mechanically exfoliated 1T-TaS_2 is placed on the bottom stage. It is moved to the

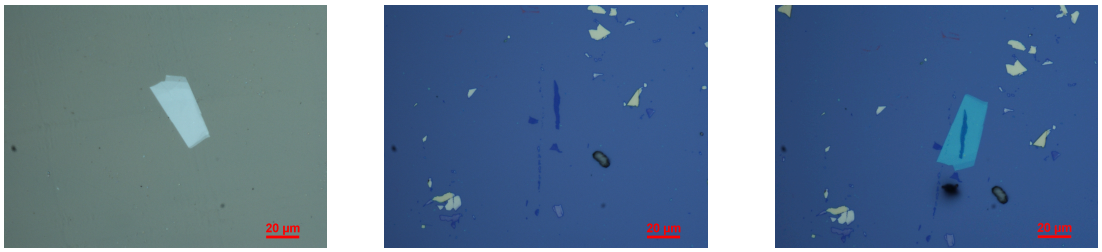

(a) (b) (c)

Figure 3.2: (a) A thin flake of hBN exfoliated on PDMS (b) A thin flake of 1T-Ta_2 exfoliated onto SiO_2/Si (c) The thin flake of 1T-Ta_2 capped with hBN after the transfer process.

field of view of the zooming lens and the focus is adjusted to the desired flake. Then the PDMS layer with the exfoliated hBN is clamped onto the top stage and roughly positioned above the sample. The focus is adjusted to find the desired hBN flake on the PDMS and the top stage is moved so that the hBN is directly above the 1T-TaS_2. By switching the focus back and forth from the hBN to the 1T-TaS_2 flake the alignment can be fine-tuned. Using the micromanipulator the top stage is gradually lowered to allow for further adjustment of the alignment between the two layers. When the alignment is acceptable the PDMS is brought in contact with the Si/SiO_2 substrate. As the pressure between the two layers increases visually there will be a change in color identifying the region where the PDMS has successfully made contact. Once there is full contact of the PDMS with the SiO_2 in the region where there is hBN on top of 1T-TaS_2 the pressure is released slowly by raising the PDMS and thus peeling the hBN [25]. Careful observation confirms the hBN has successfully adhered to the 1T-TaS_2 and SiO_2/Si substrate. Figure 3.2 illustrates this process. (a) shows hBN on the top layer (PDMS), (b) shows a 1T-TaS_2 flake on a SiO_2/Si substrate, and (c) shows the final Si / SiO_2 / 1T-TaS_2 / hBN heterostructure.

It should also be noted that increasing the temperature of the substrate during

transfer can be helpful because it reduces the viscosity of the PDMS upon contact making it more fluid and easier to adhere to the target substrate. PDMS is known to have temperature-dependent mechanical properties. The variability in viscosity with respect to temperature makes it easier to handle the PDMS stamp and control the transfer process. Additionally, heating can also increase the surface energy of the PDMS, which can improve the adhesion between the PDMS and the target substrate, leading to a more reliable transfer.

3.5 Device Fabrication Steps

After capping the 1T-TaS_2 crystal with hBN, the next step is device fabrication, which involves precise alignment. The accuracy of electrode and pad placement is critical, as patterns have fine structures. First, alignment markers are created, followed by lithography for electrodes and pads. However, since the sample is now capped with hBN, an additional step is required - etching the hBN layer. This must be followed immediately by metal deposition. The final step produces the fully assembled device, featuring a 1T-TaS_2 channel and hBN protective layer.

3.5.1 Designing Alignment Grid

To create the desired patterns on the sample, a computer-aided design (CAD) program is used. The grid encloses an area of $300 \times 300 \mu m$. Dashed lines represent the areas that will be exposed, whereas solid lines are interpreted as lines to be exposed (not the areas). The alignment markers within the grid are designed to surround the capped flake

in a way that facilitates SEM alignment. To create alignment markers using electron-beam lithography (EBL), the sample is initially coated with an e-beam resist layer (PMMA), followed by the electron-beam writing step. Then the pattern is developed using a mixture of solvents.

3.5.2 Spin Coating Resist Layer

In this step, a layer of e-beam resist is applied to the sample using spin coating with polymethyl methacrylate (PMMA). PMMA is a common positive resist and when exposed to an electron beam, it becomes more soluble in the developer solution. However, if the PMMA is highly exposed to the electron beam, it becomes a negative-tone resist where the exposed areas become polymerized and crosslinked, making them difficult to dissolve in the developer [29]. To achieve the desired thickness of the PMMA layer, it is important to consider the PMMA dilution, spinning speed, and time. The appropriate spin speed can be chosen by checking the curves of film thickness versus spin speeds based on the material's datasheet. The PMMA resist used in this work is 950 PMMA A4, and the final spinning speed is set to be 4000 rpm for 45 seconds, providing almost 200 nm film thickness based on the datasheet curves [30]. The spin coating is then followed by a baking step, where the substrate is placed on a hot plate and baked for one minute at $180°C$ and cooled for one minute. Two layers of PMMA are used for a film thickness of almost 400 nm.

3.5.3 Electron Beam Lithography

Electron-beam lithography is a process that uses an electron beam to draw patterns on resist-coated samples. This technique offers high diffraction-limited resolution, making

it ideal for nanoscale pattern writing. In EBL, a direct writing method is used where a small portion of the electron beam is separated and directly written on the resist-coated sample, eliminating the need for mask production. Although this approach provides high resolution, it can be time-consuming as the exposure is done one pixel at a time. Despite this limitation, the benefits of direct writing without a mask make EBL a popular choice for creating precise patterns for microelectronic devices.

The direct writing mode of EBL consists of several components, including a source of electrons, a set of focusing optics, a blanker for turning the e-beam on and off, a deflection system for moving the beam, and a sample holder stage [31]. Overall, EBL is a combination of scanning electron microscopy (SEM) and the nanometer pattern generation system (NPGS), which provides an environment for designing and controlling the writing steps.

In the SEM system, electrons are accelerated through the column with a voltage ranging from 0.5 V to 30 kV. Lenses implemented through the column modify the beam diameter and perform focusing, while a series of apertures define the size of the hole that the e-beam passes through. The specimen is located in the bottom chamber and brought to an appropriate working distance (WD). When the e-beam interacts with the sample, signals are generated that need to be detected and processed to form the final image. Both the gun chamber and the specimen chamber need to be highly vacuumed, with the pressure in the specimen chamber at about $10^{-4}Pa$ [32].

The first step in the EBL system is to focus on the substrate using the SEM. To do this, a prepared, resist-coated sample is placed on an SEM specimen stub fixed with carbon tape. The rough position of the capped sample is found via SEM, using the big alignment

markers previously made with photolithography. It is important to avoid increasing the magnification too high or zooming in on the specified crystal as this could damage it, given that the surface is being scanned with an e-beam.

Several SEM parameters need to be adjusted to achieve desired lithography results. For example, an acceleration voltage of 20 kV and a 20 μm aperture size is used for writing the small alignment markers. The WD, which is the distance between the surface of the specimen and the lower part of the lens, is set to 6 mm to attain good writing. By carefully adjusting these parameters and following proper techniques, EBL can be used to create highly precise patterns on the nanoscale.

Before writing patterns, it is crucial to ensure the SEM image is well-focused. Centering the aperture is another important factor in SEM setup. Most SEMs have a "wobble" mode, where the focus is altered back and forth. Poorly centered apertures can cause the image to oscillate when the wobble mode is on. By adjusting the aperture knobs for X and Y directions, the swinging behavior can be reduced and optimized. Once the aperture is aligned, the wobble mode should be deactivated.

Astigmatism is another factor that requires special attention, especially when writing fine features. It is critical to minimize astigmatism in the beam before writing patterns; otherwise, the quality of exposed lines will differ along various orientations. Astigmatism refers to an aberration or distortion that occurs in the electron beam, causing it to be focused differently in two perpendicular directions. This results in a non-uniform magnification across the image, with certain regions appearing more blurred or distorted than others. To fix astigmatism, it is recommended to focus on a part of the substrate near the

specified crystal. Then, the magnification can be increased, and the stigmator knob along the X direction can be adjusted to optimize it before refocusing. Once the optimized focus and astigmatism along X are found, the same process can be repeated for the Y direction.

The exposure dose in EBL is a crucial factor that depends not only on the resist's sensitivity but also on various other factors such as beam energy, pattern's line width, and density. Therefore, it is necessary to conduct a dose test to determine the optimum dose for pattern elements before writing on the actual sample. If the dose is not set correctly, underexposed or overexposed areas may appear in the patterns. In some cases, a poorly focused beam can result in underexposed areas, which can be resolved by adjusting the focus rather than increasing the dose [33].

3.5.4 Developing Electron Beam Resist

After using PMMA as a positive resist in EBL, the exposed areas become more soluble in a specific solution called developer. In this case, the optimal developer is a mixture of methyl isobutyl ketone (MIBK) and isopropyl alcohol (IPA). MIBK is an organic compound that is a strong solvent for PMMA and is diluted with IPA. To develop the sample, a 1:3 mixture of MIBK and IPA is applied for one minute at room temperature. The sample is then rinsed with IPA for another minute and dried with nitrogen gas.

3.5.5 Drawing Small Alignment Markers, Electrodes, and Pads

Once the alignment grid has been developed an optical image of the device can be used to properly place the alignment markers, the electrodes, and the pads. This is done by first aligning the alignment grid seen in the optical image of the device and the alignment

grid in the Design CAD program. Both a 20x and a 50x optical image are used and aligned to ensure proper alignment of the small alignment marks, electrodes, and pads and to notice small features on the heterostructure and the surrounding area. Then the center is defined as one of the larger, numbered alignment markers near the flake. The drawing steps are shown in Figure 3.3.

For the electrodes and pads to be in the correct position small alignment marks are needed. The Design CAD program is used to create the markers and position them in close enough proximity to the desired flake. The small alignment marks should be positioned in an "L" shape to ensure the x and y components are properly aligned and to account for any uncertainty in the rotation of the sample. The markers should be placed as close to the flake as possible without coming into contact they should also be out of the way of the electrodes and the pads. The small alignment markers are shown in Figure 3.3 (a) with the defined center in the top left "01".

The electrodes are then created in the desired geometry. They should be placed on top of the optical image of the 1T-TaS_2 flake capped with hBN with the desired channel length. Electrodes should be out of the way of any contaminants or non-uniformity in the PMMA resist. Since electrodes are placed in close proximity to one another one should be mindful not to allow any shorting of the contacts from other 1T-TaS_2 flakes and other debris.

Pads are larger features connected to the electrodes used to land probes for electrical measurements. They should be created large enough for the probes to land on, but also small enough so that they remain separated from one another. To help support the

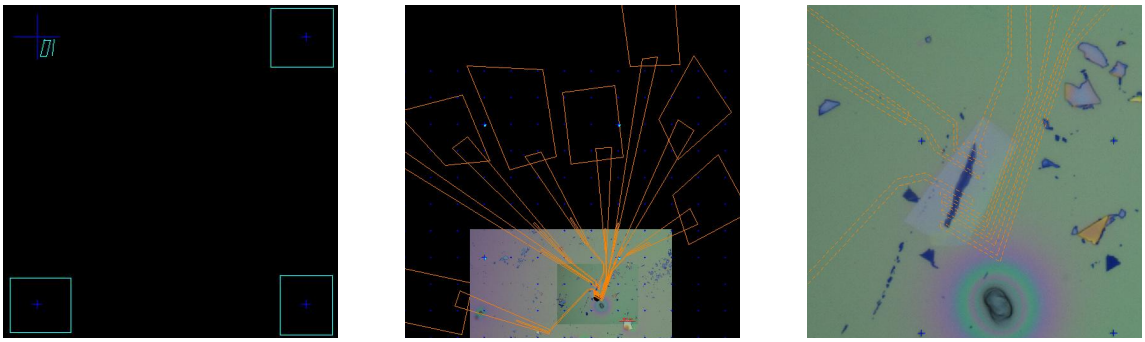

(a) (b) (c)

Figure 3.3: Design CAD is used to create the alignment grid, the small alignment marks, the electrodes, and the pads (a) Small alignment marks (teal) and center "01". The dark blue ticks show the alignment grid and the teal rectangles show the area that will be scanned to assign the alignment marks. (b) An optical image of the device (after alignment marks have been made with EBL and revealed after development) is used to assign the center and create the alignment marks, electrodes, and pads. Here the electrodes are placed on the 1T-TaS_2 flake capped with hBN and connected to the larger square pads using the alignment grid as a reference. (c) Zooming in gives a closer look at the electrodes (yellow dashed lines) on the 1T-TaS_2/hBN heterostructure. Dashed lines represent areas that will be exposed to the EBL.

electrodes a triangular portion extends from the rectangular pad to connect the pad to the electrode. This added feature helps preserve the lifetime of the devices and allows for better electrical contact. An example of the drawn electrodes and pads on an hBN capped 1T-TaS_2 devices is shown in Figure 3.3 (b) and (c). It should be noted that ".dc2" files for alignment marks, electrodes, and pads are saved separately and imported to the run file as they have different parameters in the NPGS for the EBL.

3.5.6 Fabricating Electrodes and Pads

Ensuring proper alignment of electrodes and pads is critical. The alignment step is essential to achieve this. To do this the SEM is used to focus on the previously defined center. Careful alignment of the center is required as inputting the coordinates is not

perfectly accurate. If the center is focused and the WD = 6 mm the run file must be updated with the new patterns and small alignment markers. Once the appropriate parameters for writing both small and large features are set in NPGS mode, and the small alignment marks are aligned the sample will be exposed to the e-beam and patterns will be created. This will be followed by the developing step, in which the soluble parts will be removed using MIBK and IPA, revealing the final pattern. Figure 3.4 (b) illustrates an example of the revealed pattern prior to the etching step.

3.5.7 Etching Hexagonal Boron Nitride

Once the resist has been developed, the exposed areas are revealed, while the covered areas remain coated with the resist. The next step involves etching the hBN layers within the electrode areas to enable contact with the 1T-TaS_2 crystals. To achieve this, an Atomic Layer Etcher (ALE) is used. The etching gas used is sulfur hexafluoride (SF_6). The parameters include a 40 sccm SF_6 gas flow, 20 mTorr pressure, and 50 W RF power. The initial etching time is set to 10 seconds, after which the sample is quickly removed and observed under a microscope to ensure that no hBN remains on the developed electrode areas. If the etch has not reduced the hBN completely the sample is returned to the ALE chamber, and the etching step is repeated for only 2 seconds. Once this step is complete, the metal deposition process must commence immediately. Etching the hBN layer exposes the 1T-TaS_2 crystal at the electrode areas to air, making it critical to minimize the exposure time and deposit metal promptly. The sample is placed in an e-beam evaporator (EBE) chamber and quickly pumped down. For these devices, 10 nm of titanium is used as an adhesion layer, followed by 100 nm of gold deposition for the metal contacts. The lift-

off process follows by soaking the sample in acetone for approximately 10 minutes at room temperature, rinsing with IPA, and drying with a nitrogen gas blow. Figure 3.4 (d) displays a device after metal deposition and the lift-off step.

3.5.8 Metal Deposition Using Electron Beam Evaporation

The next step is to deposit metal onto the beam-exposed areas using an electron-beam evaporator (EBE), which is a common method of physical vapor deposition. The EBE contains several sources of materials such as titanium, nickel, aluminum, chromium, and gold. Once the pressure reaches less than 4×10^{-6} torr, the selected source material is heated using a focused electron beam until it melts and evaporates. When the desired evaporation rate is meet, the shutter covering the source material is opened, and the evaporated atoms travel at high velocity deposited onto the surface of the sample. In this work, a 10 nm layer of titanium (Ti) was deposited as an adhesion layer, followed by a 100 nm layer of gold (Au). The titanium layer prevents the gold from falling off the surface. This is because titanium has an affinity for oxygen and can form a stable oxide layer on the surface of the SiO_2 substrate. Also, the lower work function of titanium is desired because it will improve the charge transfer between layers. When the desired thickness is reached, the shutter is closed to stop deposition, and the sample is removed after venting the chamber.

3.5.9 Lift-Off Process

After the metal deposition, the entire sample surface is coated with layers of metal. To remove the metal from the areas on top of the PMMA, a lift-off step is required. Before proceeding with lift-off, it is necessary to inspect the patterns under a microscope to assess

the lithography quality. Acetone is a commonly used solvent to remove PMMA resist layers, and it dissolves the layers while leaving the metal layers intact on the patterned areas. Soaking the sample in acetone for about 10 minutes at room temperature dissolves the PMMA and the metal on top of the PMMA is easily removed and the electrodes are revealed. Afterward, the sample is rinsed with IPA and dried with nitrogen gas. Figure 3.4 (d) displays a capped crystal of 1T-TaS_2 with Ti / Au electrodes after the successful liftoff.

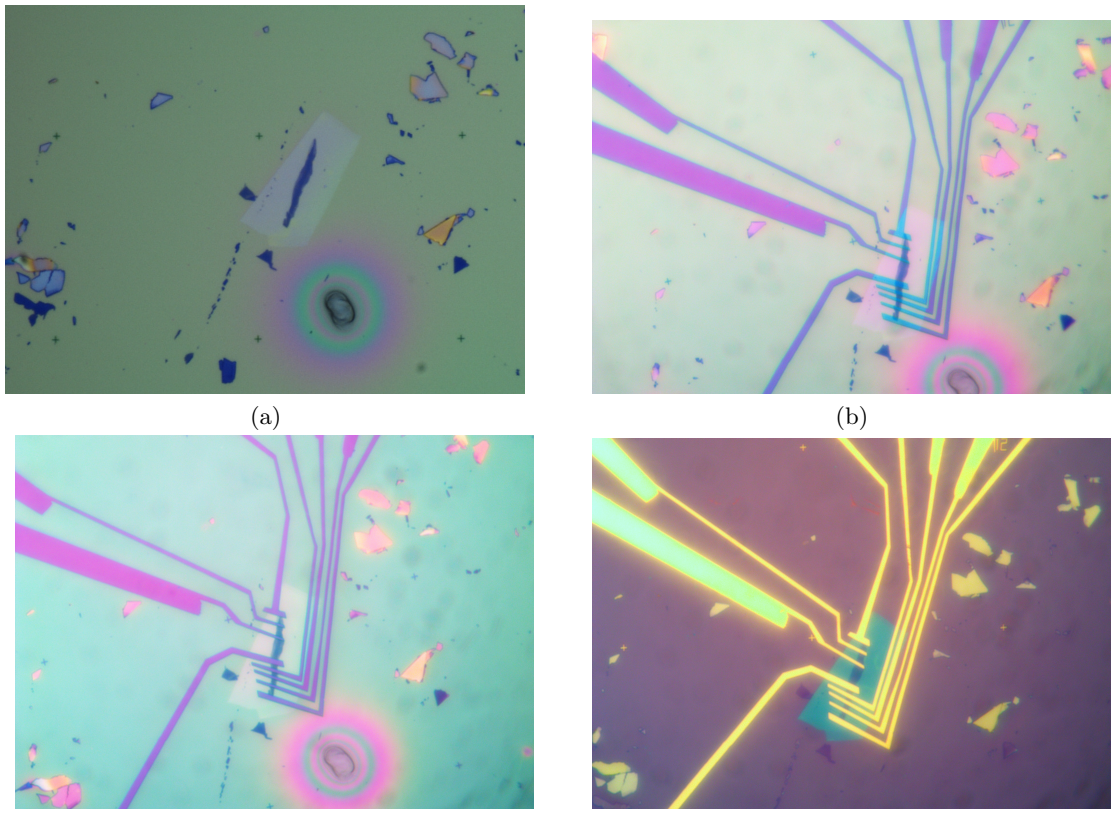

(a) (b) (c) (d)

Figure 3.4: (a) A thin flake of 1T-TaS_2 (thin purple) on SiO_2/Si is capped with hBN (teal). PMMA A4 is spin-coated and baked on the substrate. Alignment marks are written with EBL and developed (b) A pattern for the electrodes and the pads is written using EBL and revealed after development. Pink regions reveal the SiO_2 and teal regions reveal the hBN through the PMMA. (c) After ALE the patterns show a uniform color understanding that the hBN has been etched through properly (d) The final optical image of a 1T-TaS_2 device capped with hBN after electrodes and pads are written with EBL, developed, Ti/Au contacts are deposited with EBE and PMMA is removed with acetone.

Chapter 4

Results and Discussion

4.1 Introduction

The charge-density-wave (CDW) phase is a macroscopic quantum state where a periodic modulation of the electronic charge density is accompanied by periodic distortions in the underlying crystal lattice [13, 17, 34, 35]. In a conductive material, the periodicity in the electron density can induce an energy bandgap, transitioning the material to an insulating state. A number of layered van der Waals materials with quasi-one-dimensional (1D) and quasi-two-dimensional (2D) crystal structures reveal the CDW phases. Many of the quasi-1D CDW materials are transitional metal trichalcogenides (TMTs), e.g., NbS_3 and TaS_3 whereas the quasi-2D CDW materials are predominantly transitional metal dichalcogenides (TMDs), e.g., 1T polymorphs of TaS_2 and $TaSe_2$. Materials undergoing CDW phase transition induced by temperature or electric bias demonstrate non-linear electrical conductivity, hysteresis in the current-voltage characteristics, and other interesting phenomena [4, 13, 17, 18, 35–40]. A CDW phase can be commensurate or incommensurate with

the underlying crystal lattice [14, 15, 41–47]. The commensurate CDW (C-CDW) phase is observed at low temperatures. It is more electrically resistive, whereas the incommensurate CDW (IC-CDW) phase is noticed at higher temperatures and is electrically conductive.

One of the most interesting quasi-2D CDW van der Waals materials is 1T-TaS_2 which has high transition temperatures to different CDW phases. Figure 4.1 (left panel) shows the 1T structural polytype of TaS_2 where the blue spheres represent the tantalum atoms, and the orange spheres represent the sulfur atoms. Figure 4.1 (right panel) presents the nearly commensurate CDW (NC-CDW) phase consisting of C-CDW domains surrounded by more electrically conductive IC-CDW regions. The C-CDW clusters form a reconstruction in the basal plane that produces an array of star-like patterns, consisting of 13 Ta atoms with perfect translational symmetry. This lattice reconstruction is considered to be accompanied by an insulating Mott-Hubbard transition that causes a gap in the Fermi surface [48–50]. The IC-CDW regions lack the translation symmetry of Ta atoms.

Below 183 K, 1T-TaS_2 reveals its C-CDW phase which contains no conductive regions. As the temperature increases the C-CDW phase breaks up into the NC-CDW phase forming conductive regions lacking translational symmetry. As the temperature reaches $\sim$ 350 K, one observes a transition to the conducting IC-CDW. Above $\sim$ 545 K, 1T-TaS_2 transitions to a metallic phase, and above 600 K the material undergoes an irreversible polymorph transition to the 2H phase [51]. It should be noted that the transition temperatures mentioned above are approximate and can change depending on the size and thickness of the film, cooling, or heating rate, applied bias voltage, irradiation, pressure, and applied gate bias [15, 16, 52].

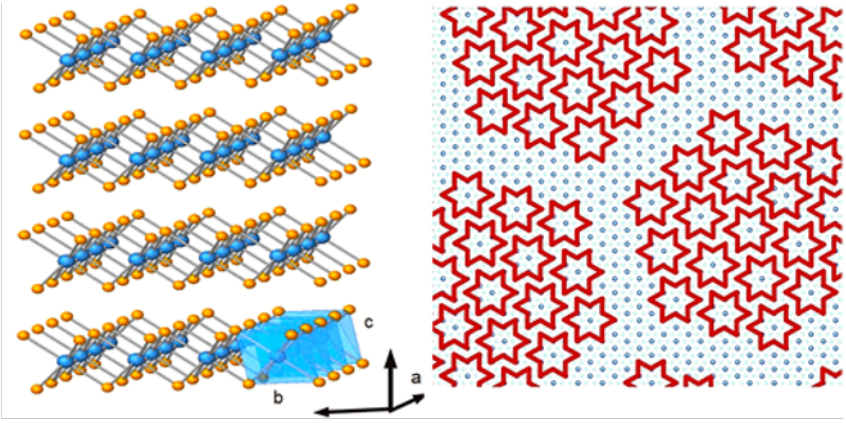

Figure 4.1: Crystal structure of 1T-TaS_2 (left panel) and schematic of the atoms structuring in the nearly-commensurate CDW phase (NC-CDW) (right panel). This figure is reprinted with permission from Jonas O Brown et al., Charge-density-wave phase transitions in quasi-2D 1T-TaS_2/hBN heterostructure devices. In Low-Dimensional Materials and Devices 2022, volume 12200, pages 16–23. SPIE, 2022 [1].

The CDW phase transitions in 1T-TaS_2 in the form of abrupt resistivity changes and hysteresis have been reported in many studies [14–16, 40, 43, 50–52]. The tunable transitions can be utilized for application in oscillators, logic circuits, neural networks, and radiation-hard electronics [15, 18, 52–55]. The demonstrated devices were implemented with two terminals to control the resistive state and the hysteresis. Tuning the source-drain current with a voltage-controlled resistor connected in series allows one to precisely control the frequency of oscillations of the CDW device [24, 56]. Other devices induce or control CDW transitions in 1T-TaS_2 with visible light or electromagnetic radiation in the MHz – GHz frequency range [24, 55–58].

4.2 Electrical Characterizations of the 1T Phase of Tantalum Disulfide

A schematic of a typical device structure is shown in the inset of Figure 4.2. Here the purple layer is the 1T-TaS_2 channel on a SiO_2 substrate, and the blue region is the hBN over the 1T-TaS_2. The current-voltage (I–V) characteristics are measured in a cryogenic probe station (Lakeshore TTPX) with a semiconductor analyzer (Agilent B1500). Figure 4.2 shows typical I–V characteristics of CDW devices with a hysteresis and resistivity change induced by applying an electric bias and passing current via the device channel. These I–Vs are consistent among many reports [24, 34, 35, 38, 59].

The hysteresis part of the I–Vs can be used to achieve desired device functionality, e.g., a voltage-controlled oscillator or an electrical switch. Figure 4.2 shows the transition between the NC-CDW and the IC-CDW phase induced by applying a voltage to a 1T-TaS_2 channel and monitoring the drain current. This switching effect is prominent from 100 K to 350 K. Above 350 K the material transitions to the IC-CDW state and the I–V slope becomes linear. An interesting feature is that the resistance is nearly the same for all temperatures after the switching point. This can be observed from the similar slopes of the I–V presented in Figure 4.2. The hysteresis window is described by the initial current jump and the final current drop V_H – V_L (see Figure 4.3 (a)). Before the initial current jump at V_H, the I-V becomes non-linear due to the Joule heating. The voltages defining the hysteresis can be fitted with an exponential component (see the inset of Figure 4.3 (a)). The temperature dependence of the threshold voltages V_H and V_L follow $V_{H,L} \propto (1 - T/T_{NC-IC})^{1/2}$ below the NC-CDW – IC-CDW transition temperature of $\sim$ 350 K (see Figure 4.3 (b)). This

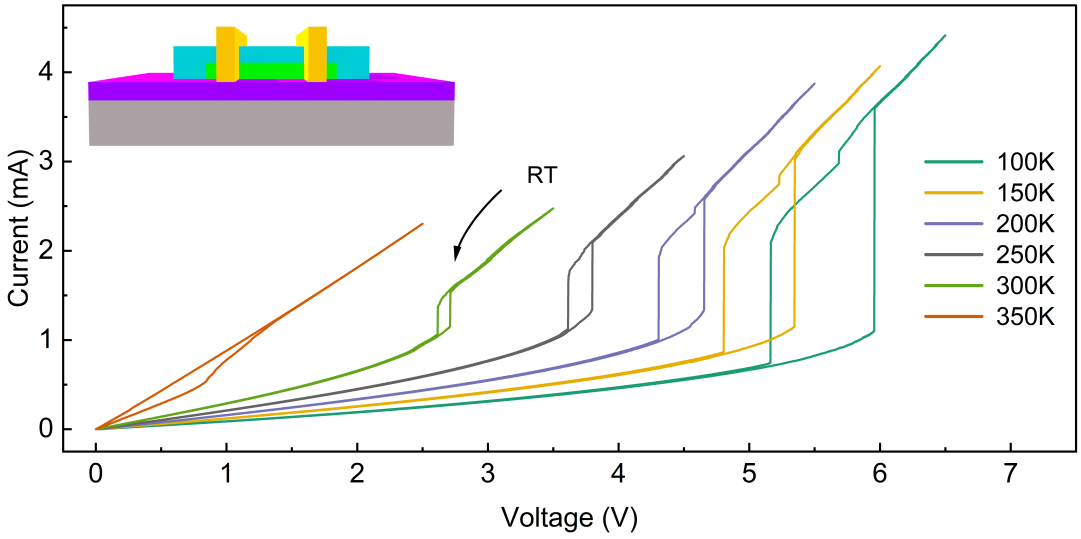

Figure 4.2: (inset) Schematic of the device, indicating 1T-TaS_2 layer (green) on a heavily p+ doped Si (grey) with 300 nm thick SiO_2 layer (violet). The layer of 1T-TaS_2 is capped with hBN (blue). The source-drain contacts (gold) are patterned using the EBL followed by the ALE to remove the hBN layer beneath the contacts. The contacts are made using the electron beam evaporation of Ti / Au with 10 nm / 100 nm thickness. I-V characteristics of a 1T-TaS_2/hBN CDW device from 100 K to 350 K. One can see the characteristic hysteresis and resistivity change induced by passing an electrical current via the device channel. This figure is reprinted with permission from Jonas O Brown et al., Charge-density-wave phase transitions in quasi-2D 1T-TaS_2/hBN heterostructure devices. In Low-Dimensional Materials and Devices 2022, volume 12200, pages 16–23. SPIE, 2022 [1].

temperature dependence is in line with analytical theories of the CDW order parameter and confirms the switching between the NC-CDW – IC-CDW phases is a true CDW effect [3].

4.3 Thickness Dependent Charge Density Wave Phase Transitions

The thickness-dependent CDW transitions in 1T-TaS_2 are important for understanding the physics and possible device applications. It has been reported that in bulk

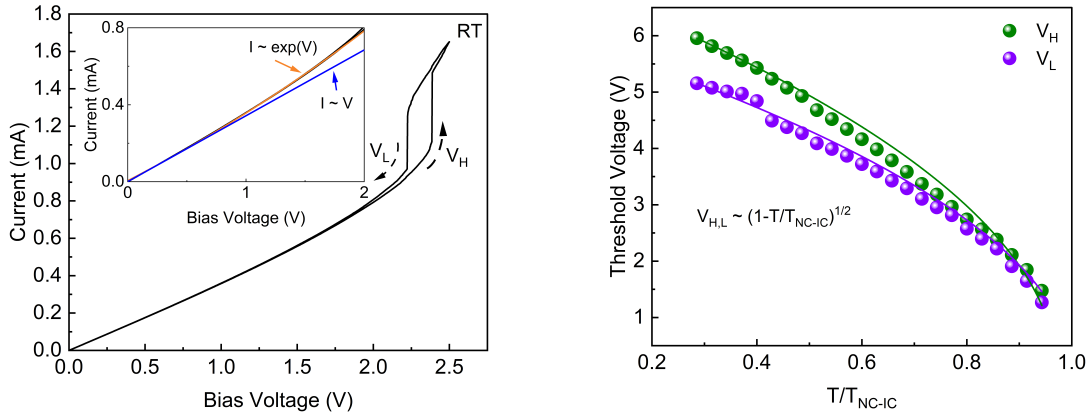

(a) (b)

Figure 4.3: (a) I–V characteristics of the same device at room temperature. The arrows show the voltage sweep direction. The hysteresis window is defined as V_H – V_L. The inset shows the current below V_H. (b) Temperature-dependent switching voltage confirms the CDW effect. Note that V_H and V_L are proportional to $(1 - T/T_{NC-IC})^{1/2}$ [3]. This figure is reprinted with permission from Jonas O Brown et al., Charge-density-wave phase transitions in quasi-2D 1T-TaS_2/hBN heterostructure devices. In Low-Dimensional Materials and Devices 2022, volume 12200, pages 16–23. SPIE, 2022 [1].

single-crystals both CDW transitions, C-CDW – NC-CDW and NC-CDW – IC-CDW, are present when adjusting the temperature [14, 16, 48, 57]. Reducing the thickness of 1T-TaS_2 below 100 nm shifts both transitions to lower temperatures during the cooling cycle. The C-CDW – NC-CDW transition vanishes at a critical thickness of $\sim$ 10 nm [14]. Below $\sim$ 3 nm an insulating state of 1T-TaS_2 has been reported [14, 16]. These critical thicknesses suggest the three-dimensional nature of CDW ordering in 1T-TaS_2. Previous studies indicated the 13-layer ($\sim$ 7.8 nm) and 3-layer ($\sim$ 1.8 nm) periodicity in the out-of-plane direction in the C-CDW and NC-CDW phases [60–64]. Periodicity arises as the layers stabilize the in-plane charge order while minimizing the sum of interlayer Coulomb and tunneling energy [14, 62].

4.4 Depinning of Charge Density Waves in Quasi-2D Materials

domain depinning of CDWs in quasi-2D materials is substantially different from that in quasi-1D bulk crystals [13]. In quasi-2D van der Waals materials, the domain depinning occurs before the switching voltage associated with the hysteresis window V_H, and before the non-linear region associated with the Joule heating. In the NC-CDW phase of 1T-TaS_2 the C-CDW clusters are surrounded by the IC-CDW regions, with no translational symmetry, which is more electrically conductive [13]. Compared with the quasi-1D CDW materials, which have relatively few normal carriers in the CDW phase, the quasi-2D materials have a large concentration of free carriers.

Sweeping through heating and cooling cycles before the NC-CDW – IC-CDW transition, the I–V characteristics of 1T-TaS_2 devices reveal a linear resistance behavior at low biases. This is in contrast with 1D structures, where the sliding of CDWs can be observed with an abrupt increase in current. The differential I–V characteristics (dI/dV) provide more insight into the domain depinning of C-CDW domains in 2D crystal structures. Figure 4.4 (a) presents dI/dV at 77K. At low voltages the fluctuations start at ~ 0.74 V for forward (V_{OF}) and reverse bias (V_{OR}) sweep. The origin of these fluctuations at low biases before the start of non-linearity can be described as the onset of domain depinning of CDWs in 1T-TaS_2 devices [13]. Here the start of the fluctuations occurs at an amplitude of $\pm$ 0.5 mA/V in the dI/dV. To further investigate the domain depinning behavior, the differential characteristics have been measured at various temperature ranges for several devices. As the temperature increases, the onset of hysteresis (V_H – V_L) in 1T-TaS_2 devices shift to

lower values, and the slope of the linear region in the I–Vs increases as depicted in Figure 4.2. These occurrences confirm the higher conductivity of the channel through the heating cycle and suggest a negative shift in the onset values of the domain depinning. Figure 4.4 (b), shows dI/dV at room temperature (300 K). For this device, the onset of fluctuations at this temperature is 0.08 V for the forward bias and 0.10 V for the reverse bias. The observed trend, which is an increase in the depinning voltage in the cooling cycle and a fall in the heating cycle, is consistent in all tested devices. One can also notice the difference in the amplitude of the dI/dV fluctuations at different temperatures. At lower temperatures, the depinning voltage occurs at higher voltages and the amplitude of fluctuations is larger than at the higher temperatures where the domain depinning occurs at lower bias voltages. In the NC-CDW regime at low temperatures, the less-conductive C-CDW domains are closely packed with thin IC-CDW boundaries. At higher temperatures the C-CDW domains decrease in size, the IC-CDW regions become thicker, and the C-CDW domains depin and begin to fluctuate [46, 65–68].

The tested devices were fabricated with thin flakes of 1T-TaS_2 ($\leq$ 10 nm), which do not show the C-CDW to NC-CDW transition owing to the small channel thickness [14]. Although this device did not undergo a complete transition to the C-CDW state, the dI/dV characteristics reveal noticeable transitions in the domain depinning voltage. In the heating cycle, the most dramatic change is between 210 K and 220 K with a shift of 40 mV in domain depinning voltage. It should be noted that this temperature is near the transition from the C-CDW – NC-CDW phase in 1T-TaS_2 during the heating cycle for bulk 1T-TaS_2 [14, 16]. Figure 4.5 (a) shows the onset of fluctuation before the transition at T=210 K for a $\sim$

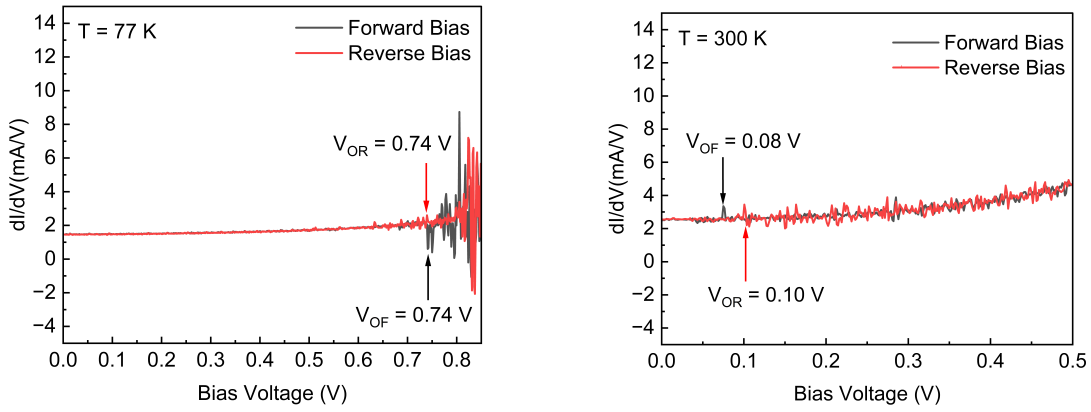

(a) (b)

Figure 4.4: Domain depinning of CDWs for different temperatures. Panels (a) and (b) depict differential I-V characteristics as a function of bias voltage for 77 K and 300 K, respectively. The V_{OF} indicates the domain depinning in the forward bias and V_{OR} is the onset in the reverse bias. This figure is reprinted with permission from Jonas O Brown et al., Charge-density-wave phase transitions in quasi-2D 1T-TaS_2/hBN heterostructure devices. In Low-Dimensional Materials and Devices 2022, volume 12200, pages 16–23. SPIE, 2022 [1].

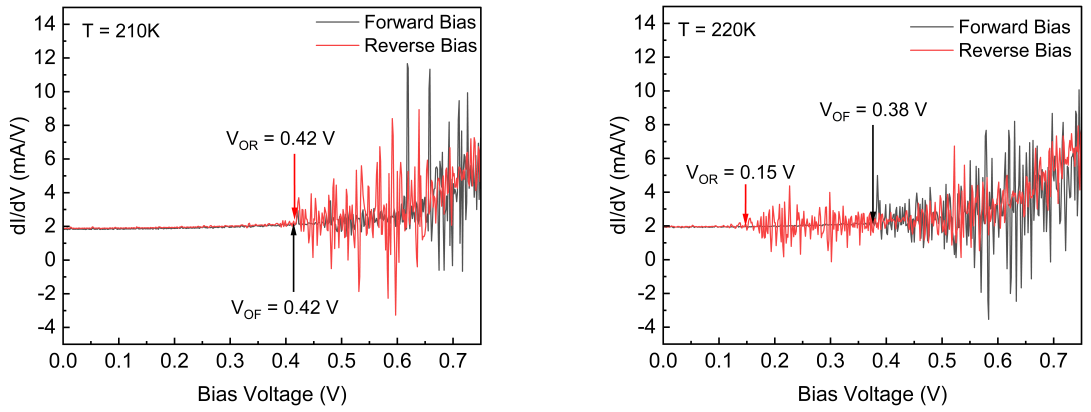

(a) (b)

Figure 4.5: Domain depinning of CDWs for different temperatures. Panel (a) and (b) compare the domain depinning voltage shifts at a temperature near C-CDW – NC-CDW transition of bulk 1T-TaS_2 in the heating cycle. As the temperature switches from 210 K to 220 K, V_{OF} shifts about $\sim$ 40 mV and V_{OR} decreases for almost $\sim$ 270 mV. This figure is reprinted with permission from Jonas O Brown et al., Charge-density-wave phase transitions in quasi-2D 1T-TaS_2/hBN heterostructure devices. In Low-Dimensional Materials and Devices 2022, volume 12200, pages 16–23. SPIE, 2022 [1].

10 nm device at V_{OF} and V_{OR} of $\sim$ 0.42 V. By increasing the temperature to T=220 K (Figure 4.5 (b)), the domain depinning voltage decreases to 0.38 V for the forward bias and to 0.15 V for the reverse bias. This change in the domain depinning near the transition temperature can result from C-CDW domains reordering and shrinking as 1T-TaS_2 enters a more conductive state. At higher temperatures near the transition to the IC-CDW phase, the domain depinning voltage goes to zero as the translational symmetry is lost in 1T-TaS_2 [13].

4.5 Temperature Dependent Study

Understanding the electrical transport properties of 1T-TaS_2 is crucial for the development of practical devices. One of the key properties that need to be studied in this context is the temperature dependence of the current-voltage (IV) characteristics of 1T-TaS_2. The IV characteristics provide insights into the conduction mechanism and the electronic band structure of the material, which can help in designing efficient electronic devices. Additionally, the temperature dependence of the IV characteristics can reveal information about the nature of the charge density wave phases. Whereas the temperature dependence of the differential IV characteristics gives rise to the nature of domain depinning. At higher temperatures in the NC phase, the domain depinning threshold can be seen at lower bias before the NC-IC phase transition. The temperature dependence of the phase transition is clearly shown by resistive fluctuations seen in dI/dV as a function of temperature and bias voltage in Figure 4.6.

Here the color map shows a boundary between green and red regions identified as

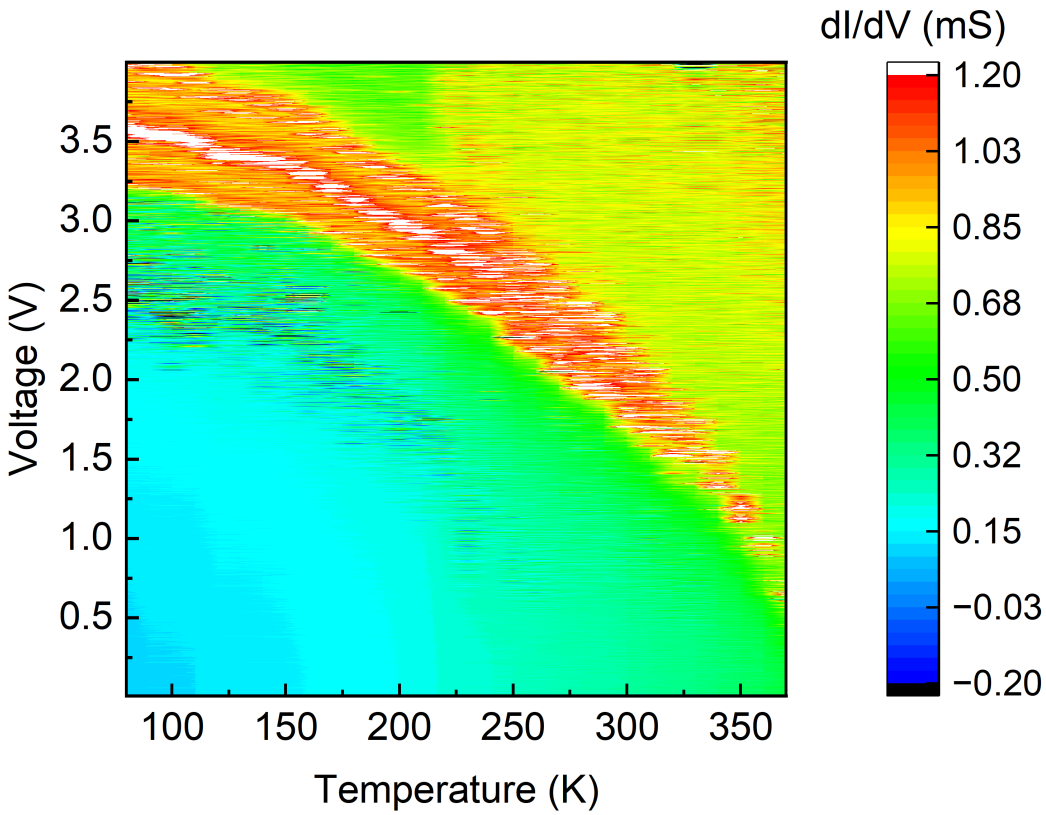

Figure 4.6: Contour plot showing the temperature dependence of the phase transition during the heating cycle for a thin device $\leq 10nm$. The NC - IC-CDW phase transition is shown as the boundary between the green and the red region.

the NC - IC-CDW phase transition. Since the device is thin $\leq 10nm$ there is no transition to the C-CDW state at low temperatures [14]. It is unclear what the black lines represent here. This negative behavior of differential conductance may allude to a meta-stable CDW state. However, more investigation needs to be done to understand this behavior more clearly. Somewhere within the NC-CDW regime, we should expect to see some signatures of domain depinning before the NC - IC-CDW phase transition. Looking closer at this region the onset of domain depinning can be understood and plotted with respect to the temperature as shown in Figure 4.7.

In this region, a decrease in the depinning threshold field with increasing temperature was observed. Both thick and thin devices are shown where the thinner devices show a larger threshold depinning voltage than thick devices. Similar to 1D devices we notice an inverse scaling with thickness in the threshold depinning voltage at room temperature. We also notice that the threshold bias for 2D materials is about 3 orders of magnitude higher than the threshold for 1D materials [69]. A take-home message is that we do have a process of understanding the depinning of domains in 2D materials, but it does not result in a sudden increase in current like that of 1D materials but rather resistive fluctuations. However, there are some similarities in that there is a similar scaling with threshold bias needed to depin the material at various temperatures.

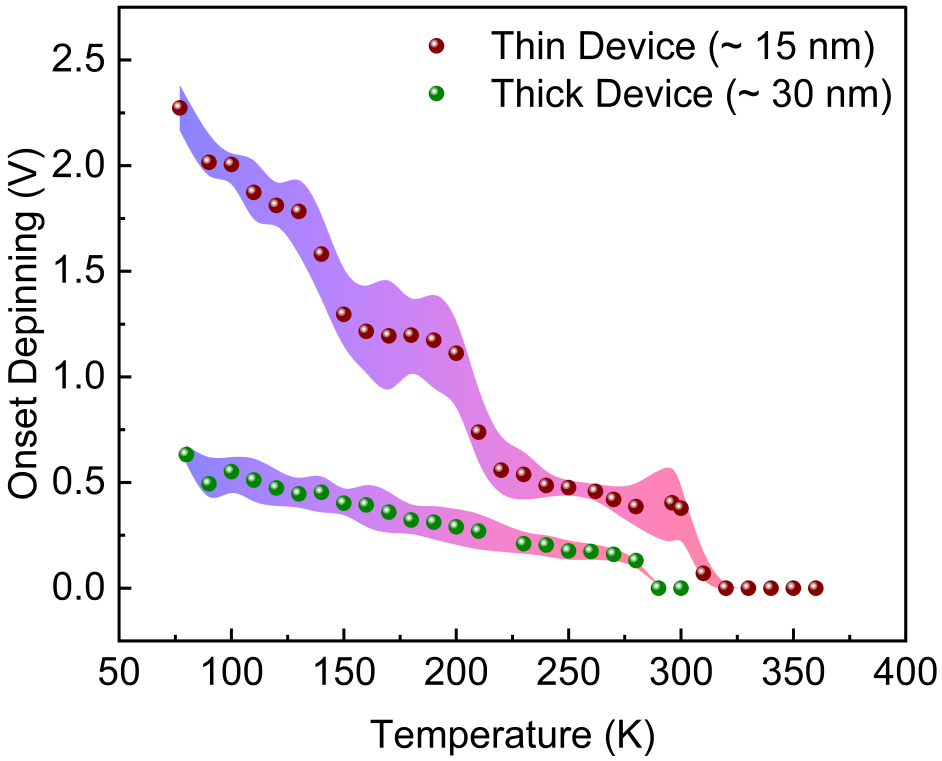

Figure 4.7: Threshold of domain depinning as a function of temperature for both thick [$\sim$ 30 nm] (green) and thin [$\sim$ 15 nm] (brown) devices. Error is understood by the uncertainty in determining the onset of the domain depinning.

4.6 Conclusions

In my preliminary results, I have reviewed the phase transitions and domain depinning of CDWs in single-crystal 1T-TaS_2 and 1T-TaS_2 / hBN heterostructure devices. It has been shown that the thickness plays a large role in both the phase transition and the onset of domain depinning in the material. Thicker devices are able to transition to the C-CDW phase whereas thin devices do not. There is also an inverse scaling with thickness for the onset of depinning. Depinning allows us to understand the movement of individual domains in the NC-CDW phase of the material giving us a new mechanism for understanding the tunable CDW structure of 1T-TaS_2. The obtained results are important for the proposed applications of the CDW in electronics and optoelectronics.

Bibliography

[1] Jonas O Brown, Maedeh Taheri, Nicholas R Sesing, Tina T Salguero, Fariborz Kargar, and Alexander A Balandin. Charge-density-wave phase transitions in quasi-2D 1T-TaS_2/h-BN heterostructure devices. In *Low-Dimensional Materials and Devices 2022*, volume 12200, pages 16–23. SPIE, 2022.

[2] George Grüner. *Density waves in solids*. CRC press, 2018.

[3] G Grüner. Density waves in solids addison-wesley. *Reading, Massachusetts*, 1994.

[4] Alexander A Balandin, Sergei V Zaitsev-Zotov, and George Grüner. Charge-density-wave quantum materials and devices—new developments and future prospects. *Applied Physics Letters*, 119(17):170401, 2021.

[5] G. Grüner, A. Zettl, W. G. Clark, and A. H. Thompson. Observation of narrow-band charge-density-wave noise in TaS_3. *Physical Review B*, 23(12):6813–6815, 6 1981.

[6] R. M. Fleming, L. F. Schneemeyer, and D. E. Moncton. Commensurate-incommensurate transition in the charge-density-wave state of $K_{0.30}MoO_3$. *Physical Review B*, 31(2):899–903, 1985.

[7] L. Forro, R. Lacoe, S. Bouffard, and D. Jérome. Defect-concentration dependence of the charge-density-wave transport in tetrathiafulvalene tetracyanoquinodimethane. *Physical Review B*, 35(11):5884–5886, 4 1987.

[8] W Einserberg, D; Kauzmann. Oxford classic texts in. *the Structure and Properties of Water*, (2005):5–13, 2005.

[9] K. S. Novoselov, A. Mishchenko, A. Carvalho, and A. H. Castro Neto. 2d materials and van der waals heterostructures. *Science*, 353(6298):aac9439, 2016.

[10] K. F. Mak, C. Lee, J. Hone, J. Shan, and T. F. Heinz. Atomically thin mos2: A new direct-gap semiconductor. *Physical Review Letters*, 105(13):136805, 2010.

[11] Q. H. Wang, K. Kalantar-Zadeh, A. Kis, J. N. Coleman, and M. S. Strano. Electronics and optoelectronics of two-dimensional transition metal dichalcogenides. *Nature Nanotechnology*, 7(11):699–712, 2012.

[12] X. Wang, Y. Gong, H. Li, X. Liang, and X. Zhang. Two-dimensional layered transition metal dichalcogenides: surface engineering and applications. *Journal of Materials Chemistry C*, 4(1):16–32, 2016.

[13] Amirmahdi Mohammadzadeh, Adil Rehman, Fariborz Kargar, Sergei Rumyantsev, Janusz M Smulko, Wojciech Knap, Roger K Lake, and Alexander A Balandin. Room temperature depinning of the charge-density waves in quasi-two-dimensional 1T-TaS_2 devices. *Applied Physics Letters*, 118(22):223101, 2021.

[14] Yijun Yu, Fangyuan Yang, Xiu Fang Lu, Ya Jun Yan, Yong-Heum Cho, Liguo Ma, Xiaohai Niu, Sejoong Kim, Young-Woo Son, Donglai Feng, et al. Gate-tunable phase transitions in thin flakes of 1T-TaS_2. *Nat. Nanotechnol.*, 10(3):270–276, 2015.

[15] Balazs Sipos, Anna F Kusmartseva, Ana Akrap, Helmut Berger, Laszlo Forró, and Eduard Tutiš. From mott state to superconductivity in 1T-TaS_2. *Nat. Mater.*, 7(12):960–965, 2008.

[16] Masaro Yoshida, Yijin Zhang, Jianting Ye, Ryuji Suzuki, Yasuhiko Imai, Shigeru Kimura, Akihiko Fujiwara, and Yoshihiro Iwasa. Controlling charge-density-wave states in nano-thick crystals of 1T-TaS_2. *Sci. Reports*, 4(1):1–5, 2014.

[17] R Samnakay, D Wickramaratne, TR Pope, RK Lake, TT Salguero, and AA Balandin. Zone-folded phonons and the commensurate–incommensurate charge-density-wave transition in 1T-$TaSe_2$ thin films. *Nano letters*, 15(5):2965–2973, 2015.

[18] Adane K Geremew, Sergey Rumyantsev, Fariborz Kargar, Bishwajit Debnath, Adrian Nosek, Matthew A Bloodgood, Marc Bockrath, Tina T Salguero, Roger K Lake, and Alexander A Balandin. Bias-voltage driven switching of the charge-density-wave and normal metallic phases in 1T-TaS_2 thin-film devices. *ACS nano*, 13(6):7231–7240, 2019.

[19] JF Revelli Jr and WA Phillips. Studies of the system TaS_2-xSe_x. *J. Solid State Chem.*, 9(2):176–186, 1974.

[20] Michael Binnewies, Robert Glaum, Marcus Schmidt, and Peer Schmidt. Chemical vapor transport reactions–a historical review. *Zeitschrift für Anorg. und Allg. Chemie*, 639(2):219–229, 2013.

[21] Z Yan, C Jiang, TR Pope, CF Tsang, JL Stickney, P Goli, J Renteria, TT Salguero, and AA Balandin. Phonon and thermal properties of exfoliated $TaSe_2$ thin films. *J. Appl. Phys.*, 114(20):204301, 2013.

[22] J Renteria, R Samnakay, C Jiang, TR Pope, P Goli, Z Yan, D Wickramaratne, TT Salguero, AG Khitun, RK Lake, et al. All-metallic electrically gated 2H-$TaSe_2$ thin-film switches and logic circuits. *J. Appl. Phys.*, 115(3):034305, 2014.

[23] K. S. Novoselov, A. K. Geim, S. V. Morozov, D. Jiang, Y. Zhang, S. V. Dubonos, I. V. Grigorieva, and A. A. Firsov. Electric field effect in atomically thin carbon films. *Science*, 306(5696):666–669, 2004.

[24] Guanxiong Liu, Bishwajit Debnath, Timothy R Pope, Tina T Salguero, Roger K Lake, and Alexander A Balandin. A charge-density-wave oscillator based on an integrated tantalum disulfide–boron nitride–graphene device operating at room temperature. *Nat. Nanotechnol.*, 11(10):845–850, 2016.

[25] Adam W. Tsen, Robert Hovden, Dennis Wang, Young Duck Kim, Katherine A. Spoth, Yu Liu, Wenjian Lu, Yuping Sun, James C. Hone, Lena F. Kourkoutis, Philip Kim, and Abhay N. Pasupathy. Structure and control of charge density waves in two-dimensional 1T-TaS_2. *Proceedings of the National Academy of Sciences of the United States of America*, 112(49):15054–15059, 2015.

[26] Chao Yuan, Jiahan Li, Lucas Lindsay, David Cherns, James W Pomeroy, Song Liu, James H Edgar, and Martin Kuball. Modulating the thermal conductivity in hexagonal boron nitride via controlled boron isotope concentration. *Communications physics*, 2(1):43, 2019.

[27] Gabriel R Jaffe, Keenan J Smith, Kenji Watanabe, Takashi Taniguchi, Max G Lagally, Mark A Eriksson, and Victor W Brar. Thickness-dependent cross-plane thermal conductivity measurements of exfoliated hexagonal boron nitride. *ACS Applied Materials & Interfaces*, 2023.

[28] Jana Martincová, Michal Otyepka, and Petr Lazar. Atomic-scale edge morphology, stability, and oxidation of single-layer 2H-TaS_2. *ChemPlusChem*, 85(12):2557–2564, 2020.

[29] Andres Castellanos-Gomez, Michele Buscema, Rianda Molenaar, Vibhor Singh, Laurens Janssen, Herre SJ Van Der Zant, and Gary A Steele. Deterministic transfer of two-dimensional materials by all-dry viscoelastic stamping. *2D Materials*, 1(1):011002, 2014.

[30] MicroChem Corp. PMMA datasheet. Datasheet, 2001.

[31] Ampere A Tseng, Kuan Chen, Chii D Chen, and Kung J Ma. Electron beam lithography in nanoscale fabrication: recent development. *IEEE Transactions on electronics packaging manufacturing*, 26(2):141–149, 2003.

[32] Peter W Hawkes and John CH Spence. *Science of microscopy*, volume 1. Springer, 2007.

[33] JC Nabity. Nanometer pattern generation system. *JC Nabity Lithography Systems, PO Box*, 5354:1996–2006, 1988.

[34] V Ya Pokrovskii, Sergey G Zybtsev, Maksim V Nikitin, Irina G Gorlova, Venera F Nasretdinova, and Sergei V Zaitsev-Zotov. High-frequency,'quantum' and electromechanical effects in quasi-one-dimensional charge density wave conductors. *Physics-Uspekhi*, 56(1):29, 2013.

[35] John Bardeen. Depinning of charge-density waves by quantum tunneling. In *Proceedings of the Yamada Conference XV on Physics and Chemistry of Quasi One-Dimensional Conductors*, pages 14–18. Elsevier, 1986.

[36] Guanxiong Liu, Sergey Rumyantsev, Matthew A Bloodgood, Tina T Salguero, and Alexander A Balandin. Low-frequency current fluctuations and sliding of the charge density waves in two-dimensional materials. *Nano Letters*, 18(6):3630–3636, 2018.

[37] Guanxiong Liu, EX Zhang, CD Liang, MA Bloodgood, Tina T Salguero, DM Fleetwood, and Alexander A Balandin. Total-ionizing-dose effects on threshold switching in 1T-TaS_2 charge density wave devices. *IEEE Electron Device Letters*, 38(12):1724–1727, 2017.

[38] Amirmahdi Mohammadzadeh, Saba Baraghani, Shenchu Yin, Fariborz Kargar, Jonathan P Bird, and Alexander A Balandin. Evidence for a thermally driven charge-density-wave transition in 1T-TaS_2 thin-film devices: Prospects for ghz switching speed. *Applied Physics Letters*, 118(9):093102, 2021.

[39] Adane K Geremew, Sergey Rumyantsev, Bishwajit Debnath, Roger K Lake, and Alexander A Balandin. High-frequency current oscillations in charge-density-wave 1T-TaS_2 devices: Revisiting the "narrow band noise" concept. *Appl. Phys. Lett.*, 116(16):163101, 2020.

[40] Adane K Geremew, Fariborz Kargar, EX Zhang, SE Zhao, E Aytan, MA Bloodgood, Tina T Salguero, Sergey Rumyantsev, A Fedoseyev, DM Fleetwood, et al. Proton-irradiation-immune electronics implemented with two-dimensional charge-density-wave devices. *Nanoscale*, 11(17):8380–8386, 2019.

[41] George Grüner. The dynamics of charge-density waves. *Reviews of modern physics*, 60(4):1129, 1988.

[42] Matthew J Hollander, Yu Liu, Wen-Jian Lu, Li-Jun Li, Yu-Ping Sun, Joshua A Robinson, and Suman Datta. Electrically driven reversible insulator–metal phase transition in 1T-TaS_2. *Nano Lett.*, 15(3):1861–1866, 2015.

[43] L Stojchevska, I Vaskivskyi, T Mertelj, P Kusar, D Svetin, S Brazovskii, and D Mihailovic. Ultrafast switching to a stable hidden quantum state in an electronic crystal. *Science*, 344(6180):177–180, 2014.

[44] B Burk, RE Thomson, John Clarke, and A Zettl. Surface and bulk charge density wave structure in 1T-TaS_2. *Science*, 257(5068):362–364, 1992.

[45] S Vogelgesang, Gero Storeck, JG Horstmann, T Diekmann, Murat Sivis, S Schramm, K Rossnagel, S Schäfer, and Claus Ropers. Phase ordering of charge density waves traced by ultrafast low-energy electron diffraction. *Nat. Phys.*, 14(2):184–190, 2018.

[46] Xian Liang Wu and Charles M Lieber. Scanning tunneling microscopy investigations of a new charge density wave phase in niobium-doped tantalum disulfide. *J. Am. Chem. Soc.*, 111(7):2731–2733, 1989.

[47] Joseph M Carpinelli, Hanno H Weitering, E Ward Plummer, and Roland Stumpf. Direct observation of a surface charge density wave. *Nat.*, 381(6581):398–400, 1996.

[48] Jl A Wilson, FJ Di Salvo, and S Mahajan. Charge-density waves and superlattices in the metallic layered transition metal dichalcogenides. *Advances in Physics*, 24(2):117–201, 1975.

[49] HW Myron and AJ Freeman. Electronic structure and fermi-surface-related instabilities in 1T-TaS_2 and 1T-$TaSe_2$. *Phys. Rev. B*, 11(8):2735, 1975.

[50] AM Woolley and G Wexler. Band structures and fermi surfaces for 1T-TaS_2, 1T-$TaSe_2$ and 1T-VSe_2. *C Solid State Phys.*, 10(14):2601, 1977.

[51] FL Givens and GE Fredericks. Thermal expansion op $NbSe_2$ and TaS_2. *J. Phys. Chem. Solids*, 38(12):1363–1365, 1977.

[52] Quirin Stahl, Maximilian Kusch, Florian Heinsch, Gaston Garbarino, Norman Kretzschmar, Kerstin Hanff, Kai Rossnagel, Jochen Geck, and Tobias Ritschel. Collapse of layer dimerization in the photo-induced hidden state of 1T-TaS_2. *Nat. Commun.*, 11(1):1247, 2020.

[53] Xuetao Zhu, Yanwei Cao, Jiandi Zhang, EW Plummer, and Jiandong Guo. Classification of charge density waves based on their nature. *Proceedings of the National Academy of Sciences*, 112(8):2367–2371, 2015.

[54] Michael Porer, Ursula Leierseder, J-M Ménard, Hatem Dachraoui, L Mouchliadis, IE Perakis, Ulrich Heinzmann, J Demsar, K Rossnagel, and Rupert Huber. Non-thermal separation of electronic and structural orders in a persisting charge density wave. *Nat. Mater.*, 13(9):857–861, 2014.

[55] Xiaoxiang Xi, Zefang Wang, Weiwei Zhao, Ju-Hyun Park, Kam Tuen Law, Helmuth Berger, László Forró, Jie Shan, and Kin Fai Mak. Ising pairing in superconducting $NbSe_2$ atomic layers. *Nat. Phys.*, 12(2):139–143, 2016.

[56] Alexander Khitun, Guanxiong Liu, and Alexander A Balandin. Two-dimensional oscillatory neural network based on room-temperature charge-density-wave devices. *IEEE Trans. Nanotechnol.*, 16(5):860–867, 2017.

[57] Chao Zhu, Yu Chen, Fucai Liu, Shoujun Zheng, Xiaobao Li, Apoorva Chaturvedi, Jiadong Zhou, Qundong Fu, Yongmin He, Qingsheng Zeng, et al. Light-tunable 1T-TaS_2 charge-density-wave oscillators. *ACS nano*, 12(11):11203–11210, 2018.

[58] DL Nika, EP Pokatilov, Q Shao, and AA Balandin. Charge-carrier states and light absorption in ordered quantum dot superlattices. *Phys. Rev. B*, 76(12):125417, 2007.

[59] Pierre Monceau. Electronic crystals: an experimental overview. *Advances in Physics*, 61(4):325–581, 2012.

[60] CB Scruby, PM Williams, and GS Parry. The role of charge density waves in structural transformations of 1T-TaS_2. *Philosophical Magazine*, 31(2):255–274, 1975.

[61] DE Moncton, FJ DiSalvo, JD Axe, LJ Sham, and Bruce R Patton. Charge-density wave stacking order in 1T-$Ta_{1-x}Zr_xSe_2$: Interlayer interactions and impurity (Zr) effects. *Phys. Rev. B*, 14(8):3432, 1976.

[62] LN Bulaevskiĭ and DI Khomskiĭ. Three-dimensional ordering of charge-density waves in quasi-one-dimensional and layered crystals. *Soviet Journal of Experimental and Theoretical Physics*, 46:608, 1977.

[63] MB Walker and RL Withers. Stacking of charge-density waves in 1-T transition-metal dichalcogenides. *Phys. Rev. B*, 28(5):2766, 1983.

[64] M Bovet, Sander van Smaalen, H Berger, R Gaal, L Forró, Louis Schlapbach, and Philipp Aebi. Interplane coupling in the quasi-two-dimensional 1T-TaS_2. *Phys. Rev. B*, 67(12):125105, 2003.

[65] Doohee Cho, Sangmo Cheon, Ki-Seok Kim, Sung-Hoon Lee, Yong-Heum Cho, Sang-Wook Cheong, and Han Woong Yeom. Nanoscale manipulation of the mott insulating state coupled to charge order in 1T-TaS_2. *Nat. Commun.*, 7(1):10453, 2016.

[66] Yaroslav A Gerasimenko, Igor Vaskivskyi, Maksim Litskevich, Jan Ravnik, Jaka Vodeb, Michele Diego, Viktor Kabanov, and Dragan Mihailovic. Quantum jamming transition to a correlated electron glass in 1T-TaS_2. *Nat. Mater.*, 18(10):1078–1083, 2019.

[67] CJ Butler, Masaro Yoshida, Tetsuo Hanaguri, and Yoshihiro Iwasa. Mottness versus unit-cell doubling as the driver of the insulating state in 1T-TaS_2. *Nat. Commun.*, 11(1):2477, 2020.

[68] Jae Whan Park, Gil Young Cho, Jinwon Lee, and Han Woong Yeom. Emergent honeycomb network of topological excitations in correlated charge density wave. *Nat. Commun.*, 10(1):4038, 2019.

[69] Z. Z. Wang, P. Monceau, H. Salva, C. Roucau, L. Guemas, and A. Meerschaut. Charge-density-wave transport above room temperature in a polytype of NbS_3. *Phys. Rev. B*, 40:11589–11593, Dec 1989.

[70] I Bloom, AC Marley, and MB Weissman. Nonequilibrium dynamics of discrete fluctuators in charge-density waves in $NbSe_3$. *Physical review letters*, 71(26):4385, 1993.

[71] G Grüner. The dynamics of spin-density waves. *Rev. Mod. Phys*, 66(1):1, 1994.

[72] Robert E Thorne. Charge-density-wave conductors. *Phys. Today*, 49(5):42–47, 1996.

[73] Sergei V Zaitsev-Zotov. Finite-size effects in quasi-one-dimensional conductors with a charge-density wave. *Physics-Uspekhi*, 47(6):533, 2004.

[74] Pradyumna Goli, Javed Khan, Darshana Wickramaratne, Roger K Lake, and Alexander A Balandin. Charge density waves in exfoliated films of van der waals materials: evolution of raman spectrum in $TiSe_2$. *Nano lett.*, 12(11):5941–5945, 2012.

[75] Sabir Hussain, Rui Xu, Kunqi Xu, Le Lei, Shuya Xing, Jianfeng Guo, Haoyu Dong, Adeel Liaqat, Rashid Iqbal, Muhammad Ahsan Iqbal, et al. Toplayer-dependent crystallographic orientation imaging in the bilayer two-dimensional materials with transverse shear microscopy. *Front. Phys.*, 16:1–8, 2021.